UNIVERSITY OF CALIFORNIA, MERCED

Study of Transport Phenomena in Flowfield and Diffusion Media of a Proton Exchange Membrane Fuel Cell

A Thesis submitted in partial satisfaction of the requirements
for the degree of Master of Science

in

Mechanical Engineering

by

Felipe E. Mojica

Committee in charge:

Professor Po-Ya Abel Chuang, Chair
Professor Ashlie Martini
Professor Min Hwan Lee

2019

This Thesis of Felipe E. Mojica is approved, and it is acceptable in quality and form for publication on microfilm and electronically:

Abel Chuang, Chair	Date
Ashlie Martini	Date
Min Hwan Lee	Date

University of California, Merced

2019

To my family; Carlos, Marielena, Felix, my friends; Viridiana, Jacob, Juan and my adviser Professor Chuang all of whom believed in me.

ABSTRACT

Proton exchange membrane fuel cells (PEMFC) are a green electrochemical technology that is rapidly gaining traction in the automotive industry and the like. Major components to the fuel cell are the flow field plates and the porous gas diffusion media (GDM) that transport reactants to, and products away from the catalyst layer where the reactions occur to produce heat water and electricity. These components can enhance or hinder fuel cell performance, efficiency, and the rate of degradation via mass transport mechanisms, especially at high power output. Our work begins with a top-level examination of the three most common flow field channel distribution patterns used in research, the parallel channel, single channel serpentine and multiple channel serpentine designs, using both computational methods and lab-built fuel cells. Using multiple channels significantly improved gas distribution across the electrode area but faced water flooding issues due to the low pressure drop. To improve transport focus was then given to the flow channel design. We designed the wavy, 2D-nozzle, and 3D-nozzle channel designs which feature alternating width, height, and direction from inlet to outlet to alter the flow path. Using the limiting current method to quantify the oxygen transport resistance (OTR) we discovered that with our 3D-nozzle design OTR reduced approximately 12% versus the straight channel design at the same current draw. Additionally, the maximum power at high humidity conditions was increased from 1.6 to 2.0 A cm^{-2} with Toray-060 GDM and 2.6 to 3.1 A cm^{-2} with Freudenberg H23C8 GDM at 0.3V. The 3D-Nozzle design has shown improved OTR and value for further investigation and optimization with the potential of use in commercial PEMFC.

TABLE OF CONTENTS

LIST OF FIGURES

LIST OF TABLES

LIST OF SYMBOLS

Chapter 1

INTRODUCTION

1.1 Background

In this section, we will discuss the motivation and background associated with this project. At the end of the section, our research objectives will be described and contents of this thesis will be outlined.

1.1.1 Motivation

The use of fossil fuels has contributed to larger levels of air pollution than any other time in human history. There have been great efforts to increase efficiency and reduce emissions, such as the development of advanced scrubbing systems in the coal power industry, use of gas electric hybrid technology in the automotive industry, and increased use of natural gas, however the problem remains. Burning coal and petroleum products will produce greenhouse gasses, CO_2 CH_4 and N_2O and particulate matter. In the short run, these reduce the clarity of our skies and pose adverse risks to human health, in the long run, these threaten the habitability of our planet by inducing global warming. There is no silver bullet to solve this problem but there is an array of technology being developed and implemented by universities and industry alike to replace fossil fuels and maintain our quality of life. One such technology are fuel cells.

1.2 Fuel Cells

Fuel cells harness the exothermic energy from one principle chemical reaction:

$$H_2 + \frac{1}{2}O_2 = H_2O \tag{1.1}$$

It does this by separating this one reaction into two half-cell reactions. The full process does vary based on the type of fuel cell but pertaining to the discussion here on out it is:

$$H_2 = 2H^+ + 2e^- \tag{1.2}$$

$$\frac{1}{2}O_2 + 2H^+ + 2e^- = H_2O \tag{1.3}$$

Hydrogen gas is flowed into the fuel cell over an anode electrode where it is reduced to hydrogen ions and electrons. The hydrogen ions transport across an electrolyte to a cathode electrode where oxygen is flowed in, while the electrons flow through an external circuit before arriving at the cathode to provide electric power to any number of electronic devices. On the cathode hydrogen ions, electrons, and oxygen combine to generate product water and heat. A fuel cell produces only heat, water, and electricity. When multiple cells are combined together to create a stack the power is sufficient to energize cars to an entire buildings with no green house gas emissions.

As mentioned, the electrochemical device known as a fuel cell comes in many different types, each primarily differ based on their operating temperature and associated electrolyte. The low temperature, less than 100°C, proton electrolyte membrane fuel cell, more often known as a Proton Exchange Membrane Fuel Cell (PEMFC) uses a solid perfluoranated sulfonic acid membrane to conduct protons. A PEMFC uses the above reaction processes and is receiving a great amount of interest for their application in the automotive industry. The low operating temperature, fast startup, and fast reaction make them well suited for providing the primary power for an automobile replacing the internal combustion engine[1–3]. The PEMFC has

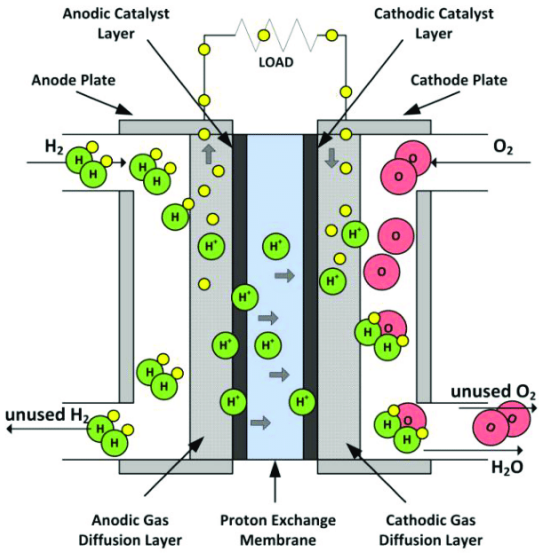

Figure 1.1: Basic architecture of a polymer electrolyte membrane fuel cell (PEMFC) [4]

several key components. In the middle of each cell is a membrane electrode assembly (MEA) composed of a proton exchange membrane in between two catalyst layers (CL) where the reactions occur. The CL structure and composition can vary

but predominantly used is a carbon supported platinum or other precious metal. Outside the CL is a gas diffusion media (GDM) that transports reactants to, and products from, the CL. These components are all sandwiched between flow fields. A flow field is a single or plurality of channels and lands that distribute the reactants and transport products across the whole active area.

1.2.1 Flow Fields

The flow field performs five essential functions 1) supply fuel and oxidant to the reaction sites, 2) remove product water, 3) transport heat 4) transport electrons, and 5) provide mechanical support to the MEA [5]. The capacity to perform these tasks can significantly impact ohmic and concentration performance losses [6–8]. A well-designed flowfield can provide a uniform distribution of reactant gases to the MEA, which is essential for homogeneous current density in a fuel cell. Non-uniform current distribution in a PEMFC can result in poor performance, lower reactant utilization, localized hot spots, mechanical stress, material degradation, and reactant starvation in the cell [9]. One of the leading causes of non-uniform current distribution is "flooding." Flooding is the condensation and accumulation of liquid water in fuel cell components and materials. As water builds up it blocks reactant pathways to reaction sites in the CL. At the same time, adequate water hydration in the electrolyte membrane needs to be maintained to provide optimal proton conductivity [10]. To balance water removal and perform the essential functions, engineers have a set of design parameters that can be modified and altered.

The design of flow fields are mainly focused on focused on (1) distribution pattern, (2) geometry of the channel cross-section, and (3) dimensions of lands and channels [11]. Distribution patterns can be described as the pathways of the channel or channels across the electrode to flow and distribute gas. The geometry of the channel, on the micron to centimeter scale, is more simply described as the shape of the channel. The lands are the areas of the flow field that are in direct contact with GDM and transport heat and electricity away from the CL via conduction.

1.2.2 Review of Flow Field Design

In the last few decades, the design of flowfields has been studies extensively [12–17], using both experimental investigation [18–20] and modeling analysis [21–23]. Some studies combined and compared their experimental results with simulation predictions to understand the fundamental mechanisms [24]. Literature show that flowfield designs, i.e. shape, size, and pattern, have a significant impact on PEMFC performance. Among all flow distribution patterns, the most commonly used are the straight parallel, single serpentine, and multiple serpentine designs [31]. An example of these three designs is shown in Figure 1.2 [25] To elucidate the impact of flowfield design on fuel cell performance, researchers have studied laboratory scale ($< 50\,\mathrm{cm}^2$) fuel cells [26]. Liu et al. compared serpentine, parallel, interdigitated, pin, and spiral

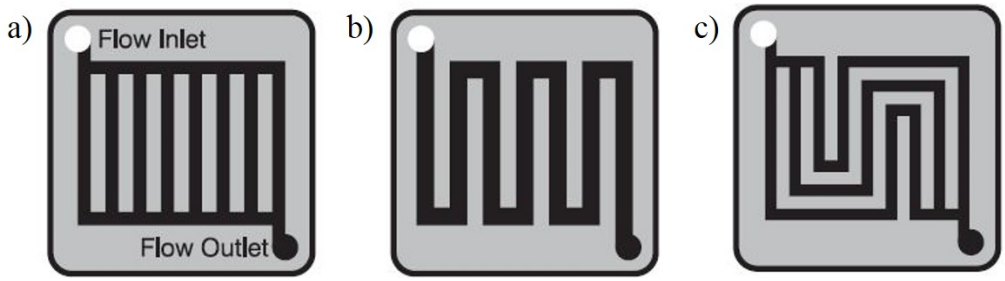

Figure 1.2: The three most commonly used flow distribution designs: a) parallel channel, b) single channel serpentine, c) multiple channel serpentine

channel design at 100% relative humidity (RH) inlet conditions and found that the serpentine flowfield design had the best performance, citing pressure drop as the key reason behind this increased performance [27]. A high pressure gradient between adjacent flow channels can induce cross flow under the rib, which aids in liquid water removal from the GDM [28] . To achieve proper water management in a PEMFC, Li et al. developed a design procedure for serpentine flow channels [29]. The design philosophy is based on the determination of appropriate pressure drop down the flow path, so that liquid water in the cells can be removed, while preventing membrane dehydration. Though pressure drop has proven to be beneficial, the additional power required from the pump or compressor to achieve the required pressure can significantly decrease overall system efficiency and increase cost [30]. This is why most fuel cell stacks for automotive applications employ parallel channels [31]. To further investigate water condensation, buildup, and removal, researchers have used invasive optical flowfield and collector plates or non-invasive neutron imaging to visualize liquid water [32, 33]. Spernjak et al., using both optical and neutron imaging, compared the transient water content in parallel, single serpentine, and interdigitated flowfields. The serpentine performed the best in this study due to high flow channel velocity, which in turn enhanced water removal in the channel [34]. Experimental studies like these are usually time and resource consuming. To save cost and facilitate design iteration cycles, simulation tools are often used for parametric study. Computational fluid dynamics (CFD) enables simulation of the effects of operating parameters, such as cell temperature, inlet RH, operating pressure, stoichiometry, and mass flow rate, on fuel cell performance [35–37]. A fundamental review of the computational modeling approaches in PEMFC research in recent years is summarized in references [38, 39].

The simplest and most straightforward design for a PEMFC flow channel is the straight square channel. Because of its simplicity to manufacture and model, it is often used as a baseline to compare other factors pertaining to performance

[40–43]. Although a facile design, it is still used in modern automotive applications. The Toyota Mirai released in 2014 uses this configuration on the anode electrode [3]. Another popular design is wavy flow channels. In this design, flow channels follow a sinusoidal wavy pattern along their length. The convex bends enhance heat transfer by inducing gas mixing in the channel [44]. Honda Motor Co. uses this design in their V-Flow stack [31, 45]. Using this design Honda reported decreased stack volume and weight, with an increased output power density by 50% and 67% respectively over their previous designs which they attributed to improved heat transfer [46]. Although stack level performance has been reported, single cell performance has not. Some other channel configurations were introduced by Ballard Power Systems in their 2003 patent, where channel depth and/or width is cycled along the channels length to induce convective flow into the GDM [47]. Alternating channel depth has been investigated. Kuo et al. developed a single-phase, steady-state CFD for a channel with spherical waves and flat troughs on the channel bottom. Their results showed that this design would increase gas velocity into the diffusion media and create uniform heat [48]. Yang et al. developed a numerical model discretized using the finite-volume semi-implicit method for pressure-linked equations consistent (SIMPLEC) method [49]. Their results indicated that a waved channel depth increases the velocity of gasses into the diffusion media and increases the concentration directly adjacent to the catalyst layer and that the total number of waves per unit length did not affect performance. Han et al performed both numerical and experimental studies of channels with wave form depth [50]. Their computational results showed that the design could delay concentration polarization by increasing oxygen concentration in the diffusion media and reported increases in max power density of 5.76% over the reference square channel flow field in $25\,\mathrm{cm}^2$ single cell experiments. The most notable non-conventional design is employed by Toyota in the Mirai, with a channel that directs gas into the gas diffusion layer. A successful design in regards to function but the complexity makes it unlikely to see widespread use.

1.3 Gas Diffusion Media

The GDM, or gas diffusion layer (GDL), has five functions in the fuel cell: 1) provide reactant passage to the catalyst layer, 2) provide pathway for product water removal, 3) conduct electrons to the catalyst, 4) remove heat, 5) provide mechanical strength. There are a variaety of GDM that have been studied and tested in PEMFC; carbon cloth [51], carbon fiber paper (CFP) [52–54], catalyst coated carbon fiber paper, metallic thin films [55] and even carbon fiber aerogels [56, 57]. The use of carbon fiber paper is the most prolific in the current literature, therefore, the rest of the GDM discussion will be in reference to CFP. The GDM should be sufficiently thin in order to reduce transport resistance of the incoming reactant. However, too thin and it can suffer losses to its mechanical properties

and increase the electrical contact resistance. Removal of liquid water also suffers if this layer is too thin [58]. The porosity of the material is a trade off between transport resistance and electrical resistance. This was demonstrated by Lee et al. in their examination of GDL compression pressure and performance [59]. Heat must be properly conducted away as well. It was observed by Baker and Caulk that the degree of conductivity can effect the location of water condensation [60]. The choice of CFP then depends on the strategy one would like to employ for the fuel cell build. Some properties for CFP are listed in Table A.3.

The CFP is made, as the name would suggest, in a roll-to-roll paper making process. Following this process other processes can be applied, such as wet proofing and the addition of a microporous layer (MPL). Wet proofing consists of immersion of the paper in a PTFE dispersion and drying to make the media more hydrophobic [61, 62]. The amount of PTFE is an optimized parameter, too much will reduce porosity and permeability and can actually be counter productive to water removal as it removes hydrophilic pathways leading out of the paper. The MPL serves as an interfacial layer between the fibrous CFP and the catalyst bed. Made of high surface area carbon fiber and a PTFE dispersion it reduces contact resistance and prevents fiber intrusion into the catalyst layer. The most important function is to aid water management, how exactly it does so is still a mater of debate. The impact of MPL contents and structure is an active area of study. The current general consensus however is that it prevents water from accumulation at that interface due to its high hydrophobicity and small pore size [63–65].

1.4 Review of Mass Transport Phenomena

The environment inside the fuel cell is a complex one. It has already been touched on in the previous sections but to encapsulate the phenomena; there are mixtures of multiple gas species, with two phase flow, and transport in solid porous media of varying, thickness pore size, and hydrophobicity. Figure 1.3 below illustrates the transport that occurs in PEMFC [66]. To begin to understand the mass transport phenomena in PEMFC, one should start at the conservation of mass and momentum.

$$\rho \nabla \cdot (\mathrm{U}) = 0 \tag{1.4}$$

The above equation is for the conservation mass also known as the continuity equation, here ρ is the density ($\mathrm{kg\,m^{-3}}$) and U is the velocity vector matrix ($\mathrm{m\,s^{-1}}$). The conservation of momentum is expressed in the Navier stokes equation as

$$\rho \mathrm{U} \cdot \nabla \mathrm{U} = \nabla \left(-p\mathrm{I} + \mu \left[\nabla \mathrm{U} + (\nabla \mathrm{U})^T \right] - \frac{2}{3} \mu \nabla \mathrm{U} \right) \tag{1.5}$$

Where p is the pressure (kPa), μ is the viscosity ($\mathrm{kg\,m^{-1}\,s^{-1}}$) and the mathematical expressions I and T are the identity matrix and transpose of the matrix respectively.

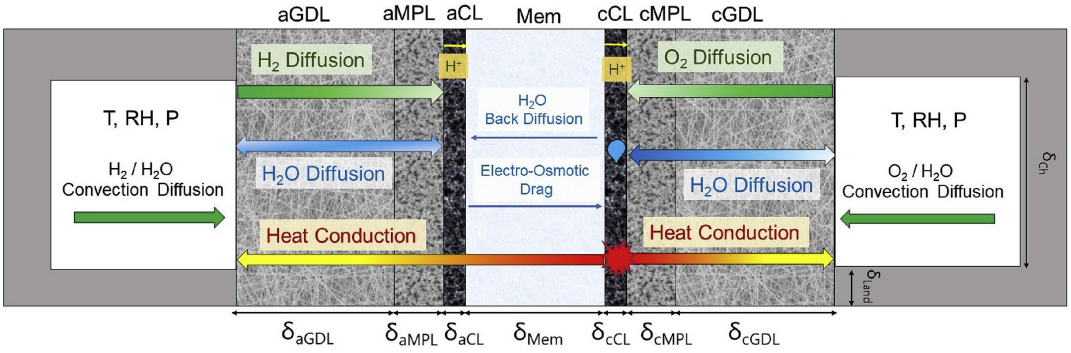

Figure 1.3: Cut away view of a PEMFC illustrating the occurring transport phenomena [66]

In the above expression continuity was expressed for a system where the no species was consumed, in the fuel cell continuity is not equal to zero as oxygen and hydrogen are consumed and water is produced in the chemical reactions at the catalyst surfaces. The rate at which each species is consumed and produced is related to the current draw I (A) by Faradays constant F ($\mathrm{C\,mol^{-1}}$) by the following:

$$Q_{O_2} = -\frac{I}{2F} \tag{1.6}$$

$$Q_{H_2} = -\frac{I}{2F} \tag{1.7}$$

$$Q_{H_2O} = \frac{I}{4F} \tag{1.8}$$

Where Q_i ($\mathrm{mol\,s^{-1}}$) is used as to express the flux of species into or out of the system. The consumption H_2 and O_2 and the production of H_2O is the driving force for mass transport transport. A concentration and pressure difference is generated and species move down the gradient via diffusion and convection.

1.4.1 Diffusivity of Gasses

Diffusion is the movement of species from a region of higher to lower conectration. The mass flux is proportional to the concentration difference over the distance between the two regions. This can be described by Ficks law of diffusion

$$N_{O_2} = \frac{i}{4F} = \frac{C_{O_2}^{channel} - C_{O_2}^{catalyst}}{R_{O_2}^{total}} = D_{ij}\frac{C_{O_2}^{channel} - C_{O_2}^{channel}}{\delta_{GDM}} \tag{1.9}$$

Where N is the molar flux ($\mathrm{mol\,m^{-2}}$) of species i, ω is the mass fraction of species i and D_{ij} is the binary diffusivity ($\mathrm{m^2\,s}$) of species i in j or vice versa.

The diffusivity for two gas components can be calculated using the Chapman-Enksog equation for diffusivity:

$$D_{ij} = \frac{3}{16}\sqrt{\frac{2RT}{\pi}\left(\frac{1}{M_i}+\frac{1}{M_j}\right)}\frac{1}{\tilde{N}\sigma_{ij}^2\Omega_{D,ij}} \tag{1.10}$$

Where R is the ideal gas constant ($\mathrm{J\,K^{-1}\,mol^{-1}}$), T is the temperature (K), M is the molecular weight($\mathrm{kg\,mol^{-1}}$). The Chapman-Enksog Kinetic theory of which this is based is derived from the Boltzman equation for one-particle distribution and gives an expression for transport properties in terms of an intermolecular potential energy. The potential energy is a function of a molecules size, distance between molecules and energy of attraction between those molecules. The full derivation and description is excluded here but can be found in reference [67].

The gas mixture on the cathode side is humidified air, a ternary mixture, for this the Maxwell-Stefan (equation 1.11), or mixture averaged diffusion model (equation 1.12) can be used to define the diffusivity of each respective gas species.

$$\nabla\left(-\rho\omega_i\sum_{j=1}^{N}\left(D_{ij}^{eff}\nabla x_j + (x_j-\omega_j)\frac{\nabla p}{p}\right)+\rho\omega_i u\right) = S_i \tag{1.11}$$

$$D_i^{\mathrm{m}} = \frac{1-\omega_i}{\sum\limits_{k\neq i}\frac{X_k}{D_{i,k}}} \tag{1.12}$$

Thus we have a diffusivity term for all gasses in the open and clear channel. In the porous media diffusivity differs as gas motion is impeded by collision with the GDM fibers and pore walls. In the large pore space of the CFP this is factored into the diffusivity by

$$D_{i,k}^{eff} = \frac{\varepsilon}{\tau}D_{i,k} \tag{1.13}$$

Where ε is the porosity, the total void fraction and τ is the tortuosity of the material. Tortuosity describes the amount of meandering a gas molecule must travel to move through the material.

$$\varepsilon = \frac{V_{void}}{V_{solid}} \tag{1.14}$$

$$\tau = \frac{\delta_{flowpath}}{\delta_{GDM}} \tag{1.15}$$

As the gas enters the smaller pores of the MPL and CL the gas molecules begin to collide more with the pore walls than other gas molecules. The mean free path

between molecular collisions is greater than the pore diameter in these regions. In this case Knudesn diffusion describes the diffusivity

$$D_{Knuden} = \frac{1}{3} d_{pore} \sqrt{\frac{8RT}{\pi M_i}} \tag{1.16}$$

Where d_{pore} is the pore diameter(m). Aside from this travel through the empty pore space diffusion may also occur through water and the thin ionomer that could be blocking the catalyst reaction sites. These phenomena is out of the scope of the following work and excluded here, but references [68–71] discusses this in further detail.

1.4.2 Convective Mass Transport

Convective mass transport occurs in PEMFC primarily in the Channel-DM region. Flow in the channel is very similar to regular flow in pipes encountered in fluid dynamics courses. The difference arises from the fact that one or more walls is a porous media where mass transfer occurs. Still much of the same analysis and principles can be applied. Starting from the Reynolds number, the ratio of inertial to viscous forces

$$\mathrm{Re} = \frac{\rho u d_h}{\mu} \tag{1.17}$$

The Reynolds in PEMFC channels is often less than 2000 due to the small diameters required, meaning that the flow is laminar. This is perhaps not the best for heat and mass transfer, but this does make modeling and analysis a simpler task. The convective mass transfer that occurs from the channel to the GDM or vice versa occurs due to local density difference and can be esitimated by

$$N_i = -h_m (C_{channel} - C_{CL}) \tag{1.18}$$

Where N is the molar flux and h_m is the convective molar mass transfer coefficient ($\mathrm{m\,s^{-1}}$) which is dependent on channel geometry, wall conditions, and physical properties of the species. The mass transfer coefficient can be found using Sherwood number, the non-dimensional ratio of convective to diffusive transport.

$$\mathrm{Sh} = h_m \frac{d_{ch}}{D_{ij}} \tag{1.19}$$

Where d_{ch} is the hydraulic diameter (m). For laminar fully developed flow the value of Sh can be found in literature for some common geometries. Determination of a local SH for a non-fully developed flow, such as at the entrance region where the boundary layer is thinner and rate of mass transfer is higher, is more complex. The convective mass transfer just discussed was for flow over the GDM, flow can also be

directed into the GDM, forced convection. In this case the flow equation must be modified to reflect properties of the porous media and their effect on impeding flow. The traditional equation for flow in porous media is Darcys equation:

$$\nabla p = -\frac{\mu}{K}\mathrm{U} \tag{1.20}$$

Liquid or gas flows down the pressure gradient and the resistance to this flow is captured by the dynamic viscosity, and the permeability K (m^2), the measure of the materials ability to allow flow through it. When using this equation however potential problems may arise form the boundary condition at the clear-porous media interface. Another equation fit for modeling the flow from the channel into the CFP is the Brinkmans equation

$$\frac{1}{\varepsilon}\rho\left(\mathrm{U}\cdot\nabla\right)\mathrm{U}\frac{1}{\varepsilon} = \nabla\cdot\left[-p\mathrm{I} + \mu\frac{1}{\varepsilon}\left(\nabla\mathrm{U} + \left(\nabla\mathrm{U}\right)^{\mathrm{T}}\right) - \frac{2}{3}\mu\frac{1}{\varepsilon}\left(\nabla\cdot\mathrm{U}\right)\mathrm{I}\right] - \frac{\mu}{\kappa}\mathrm{U} \tag{1.21}$$

This version of Brinkmans equation is essentially a modified version of the Navier-Stokes equation. This fact makes matching conditions at the channel-GDM interface less troublesome and can take into account the no-slip boundary condition [72].

1.4.3 Two phase Flow

Given the relatively low operating temperature of the PEMFC ($< 100°\mathrm{C}$) the formation and removal of liquid with simultaneous maintenance of proper water balance is an important area of research. Water can condense anywhere in the cell given the correct local conditions. GDM flooding starts at hydrophilic seed sites forming small droplets known as the pendular condition, as it grows along the fibers it enters the funicular condition, finally once water completely fills the pore it enters the saturated condition. The total saturation in the GDM can be defined as the volumetric ratio of liquid filled pores to the total pore volume. The water formed in pore then extends to other pores and forms tendrils that extend through the GDM [73]. The movement of water in porous media controlled by viscous and capillary forces. The capillary effect is a combination of surface and and wall adhesion in small pores [74]. The capillary pressure can be defined as

$$p_{capillary} = p_g - p_{liq} = \frac{4\sigma_{lq}\cos\theta}{d_{pore}} \tag{1.22}$$

Where p_g is the gas pressure p_{liq} is the liquid water pressure, σ_{liq} is the surface tension coefficient of liquid water ($\mathrm{N\,m^{-1}}$), d is the diameter of the liquid filled pore and θ is the contact angle . Increasing the contact angle, increasing the hydrophobicity, reduces the contact are of water on the pore wall increasing the capillary pressure

gradient. Liquid water will then move by capillary fingering until it enters the channel emerging from the GDM as a droplet.

Once the droplet is in the channel transport it can begin to move and flow to the outlet. This flow can take on different patterns depending on channel conditions and the amount of water injection. Wilkins and Liu describe these patterns based on the size of the body of water as, droplet, film, or slug flow. The movement of these bodies is induced by pressure and shear forces by the gas flow in the channel [75, 76]. The simple model by Chen et al. for water droplet removal is: [77] here

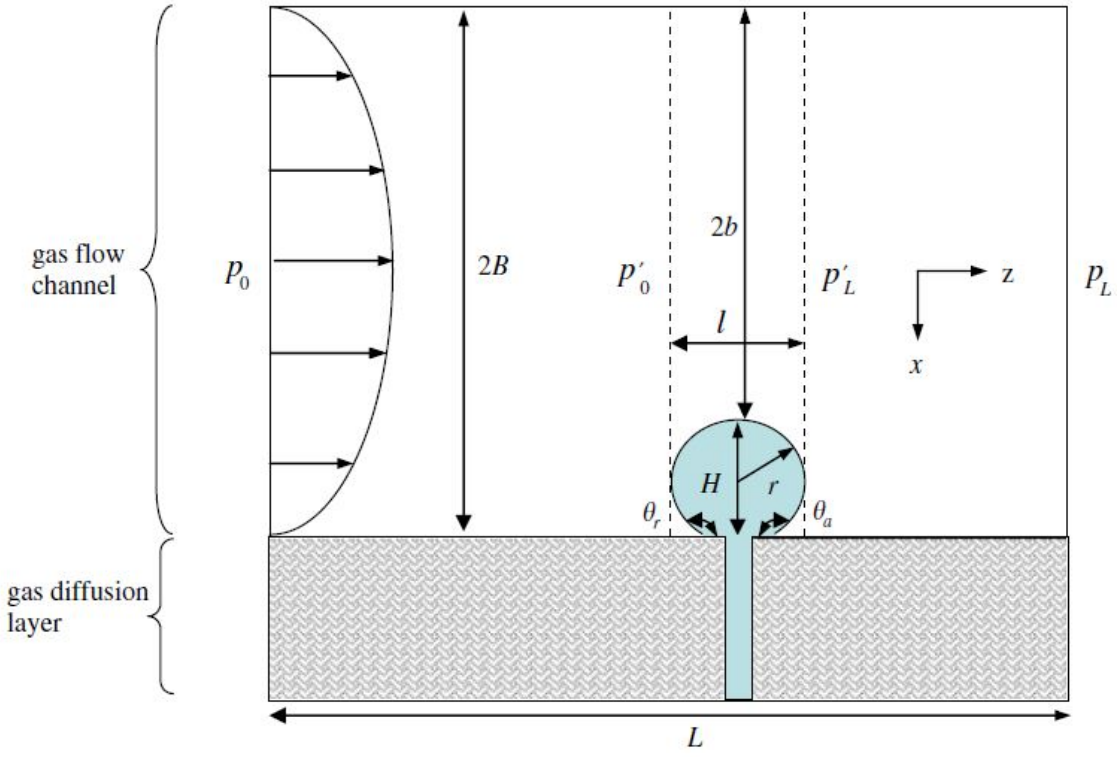

Figure 1.4: Control volume enclosing the water droplet, dimensions follow Chen's original variable assignment [77]

p_0 is the upstream pressure, p_l is the downstream pressure, $2B$ is the height of the channel, $2b$ is the distance between the top of the water droplet and the top of the channel, L is the characteristic length, l is the length of the emerging droplet, H is the normalized height of the droplet and r is the radius. The angles $\theta\theta_r$ and θ_a are the upstream and downstream contact angles respectively. To move the droplet the

drag force must be greater than the GDM wall adhesion force.

$$F_{drag} = \frac{48\mu_{gas}\mathrm{U}B}{(1-\cos(\theta_a))} \times \frac{(1+H)H^2}{(1-\cos(\theta_a))(1+H)^3 + (4B/L)H\left[1-(1-H)^3\right]}$$
$$> \tag{1.23}$$
$$F_\sigma = \sigma\cos(\theta_r)\frac{\pi D\sin(\theta_a)}{2} - \sigma\cos(\theta_a)\frac{\pi D\sin(\theta_a)}{2}$$

This model was derived for water removal in the channel but can also be applied in the GDM by exchanging channel height with the pore size, and the characteristic length with the fiber length.

1.5 Research Objectives and Thesis Outline

As society begins to use PEM fuel cells for it's energy needs it is necessary to fully investigate how components like flow fields and the GDM impact performance. Further, since fuel cell operation is multiphysics phenomena, it is essential to study how operating parameters can impact fuel cell performance.

From the literature it has been shown that the three most common designs for flow channel distribution, parallel, single serpentine, and multiple serpentine. These have been studied to an extent separately, however, not altogether using both experimental and simulation methods. It has been shown in the literature that improving channel designs can enhance transport of reactants to the catalyst and subsequently fuel cell performance. However, transport resistance from a comprehensive experimental study has not been reported.

This research aims to improve the fundamental understanding of how flow field design affects fuel cell performance through experimental and computational analysis. We do this by first, examining the characteristics of three common flow channel distributions and the interplay of performance and operating parameters. Second, we narrow the scope to channel design and it's impact on oxygen transport resistance. Finally, while examining the impact of channel design we design, fabricate, and test a novel 3D-nozzle that has very promising performance and can improve transport.

The first chapter of this thesis provides a background on fuel cells, the relevant components of this study, and the associated transport phenomena on which our research is based. Chapter 2 describes the experimental equipment used for diagnostics. Chapter 3 is a study on the three common flow field channel distributions and the effect of given cell conditions. Chapter 4 is a study of four flow channel designs examining their effect on oxygen transport resistance. The last chapter, Chapter 5, provides summary and conclusion of these studies and proposes future research.

Chapter 2

EXPERIMENTS

2.1 Materials

Commercialized MEAs made by Ion Power, Inc. were used for all experiments. The details of the MEA specifications are Nafion NR-211 membrane of 25 µm thickness with electrode area of 5 cm^2 and loading of 0.3 mg cm^{-2} platinum loading on both anode and cathode. Symmetric material design was employed on both anode and cathode sides. Experiments with varied material, flow field and GDM, on anode side were tested however the observed impact was not significant, and thus excluded here. For experiments where the active area was less 2 cm^2 the electrode area was obtained by masking the additional electrode area with PTFE gasket.

The GDM used in these experiments were Sigracet SGL 29-BC, Toray 060, and Freudenberg H23C8. When assembled the GDM is compressed some by the flow field. It has been studied and reported for specific GDM a set amount of compression yields the best trade off between porosity and electrical conductivity [78]. The compression can be applied by a set amount in one of two ways, the first is if a compressible rubber gasket material is used to seal the cell a set amount pressure is applied to the end plates via the tie rods or other clamping mechanism. Second, the gasket is nearly incompressible and is of a set amount of thickness to achieve the strain. In this study, the gasket was PTFE, which compresses only 5%, the second case. The target strain for the GDM used in this study is in Table 2.1. As the PTFE gasket material is sold in 1 mil thicknesses increments and there is some inconsistency to advertised material film thickness the PTFE gasket material is selected so as to be within 1.5% of the target strain.

2.2 Equipment

This section details the laboratory equipment used to carry out fuel cell testing.

2.2.1 Fuel Cell Test Station

The experimental testing was done using a precise-controlled automated fuel cell station manufactured by Greenlight Innovation [18]. All gases used, hydrogen, nitrogen, and air, were of 99.99% purity from Praxair Inc.

2.2.2 Potentiostat and Galvanostat

A Gamry Refererence 3000 with 30K booster potentiostat/galvanostat was used to perform electrochemical impedance spectroscopy (EIS). This is an in-situ technique that adds an AC electrical signal on top of the DC load and measures the following response. It is used here to measure the high frequency resistance (HFR) of the tested cell [79, 80]. In addition, the Gamry Reference 3000 was also used to perform cyclic voltammetry, a technique to measure the shorting and crossover currents, and the electrochemical surface area of each cell. More detail on these techniques is provided in appendices A.1 and A.2.

2.3 Experiment Cell Assembly

Each fuel cell was built with the aforementioned material in the following manner. Selected gas diffusion media was cut to size ($5\,cm^2$ or $2\,cm^2$) with a cutting die. The GDM was placed on the blades of the cutting die, an acrylic plate was then placed on top of the GDM and all three were placed in a press. The press was hand cranked to cut the GDM and pressure was then released and the GDM removed. Any compression of the GDM by the cutting process was negligible and did not show as a change in thickness of the material when tested. Once cut, the material's thickness was measured To clean and remove any oils and dirt on the collector plates, flow field plates, and gasket materials were rinsed once with an organic solvent such as isopropyl alcohol, then once with deionized water to remove any solvent that did not immediately evaporate. This ensured no solvent remained and prevented any from coming into contact with the MEA that could possibly dissolve some of the catalyst support. The components were then allowed to air dry.

GDM	Strain (%)
SGL-29BC	26
Toray 060	22
Freudenberg H23C8	17

Table 2.1: Target strain rate for gas diffusion media used in this study

MEA were removed from their original packaging and placed flat on a cutting board. A clean 1/8" hole punch is then used to create holes for alignment pins. The cell was then assembled with single cell hardware produced by Fuel Cell Technology Inc. as shown in figure 2.1 with the flow field design to be tested.

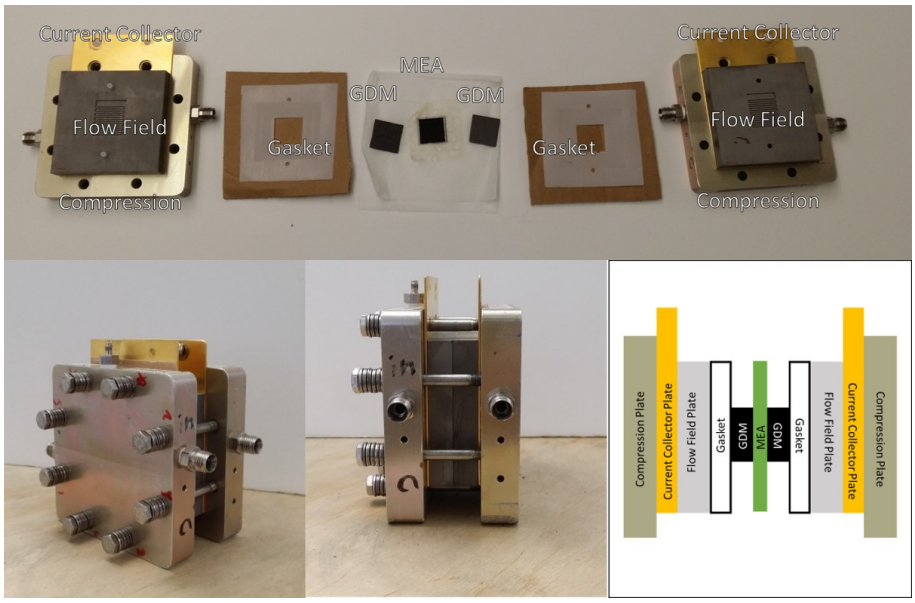

Figure 2.1: Assembly of cell from the outside moving towards the center are the compression plates, current collectors, flow fields, gaskets, GDM, and MEA

Eight bolts were inserted and torqued to 50 in-lbs in increments of 10 in-lbs to avoid unequal compression. The cell was then tested for shorting using a Fluke 117 multimeter. If the resistance measured increased from a low value, below roughly 10 Ohm to above 120 Ohm, an indication of charge building on the electrode, it was determined that shorting across the membrane was not present. The cell was then placed on the test stand and connected to the inlet and outlet connections.The pure hydrogen, nitrogen, and air cylinders were opened with an outlet pressure of 100 psi. Industrial quality nitrogen and building air supply were also opened and connected to the test station to control station back pressure. Proper sealing was tested by flowing pure nitrogen into anode and cathode and then setting pressure to 50 kPa gauge. Once flow was cut, if the the pressure on anode or cathode did not show a linearly decreasing pressure greater than $1\,\mathrm{kPa\,min^{-1}}$ then the cell was considered sealed and free of detrimental or unsafe leak. With leak check completed the thermocouples (TC), voltage senses, load bank control, Gamry senses were connected, the heater cartridges inserted into the end plates, and the cooling fans placed facing the end plates. Following the assembly the protocol was initiated via the automated test scripts for the associated tests in Chapter 3 and 4.

2.4 COMSOL Modeling

COMSOL Multiphysics®, a finite element physics modeling software is used to generate 3D steady state, single phase models to examine the influence of flow fields on species distribution. The use of this commercial software allows possible future studies to build off this existing model for incorporation of other physical phenomena. Additionally, it has been used with success by other fuel cell researchers [81–84]. The models here were formulated from the conservation principles of charge, species, mass and momentum. The basic assumptions for the computational model were: 1) the PEMFC operates under steady-state conditions, 2) all reactants and products are in gaseous phase and follow ideal gas law, 3) the flow in the gas channel is laminar, 4) the electrochemical reaction when included occurs only in the catalyst layer (CL), 5) the GDLs, CLs, and membrane are isotropic and homogeneous, and 6) no crossover of reactant gases and water through the membrane occurs.

2.4.1 Mass transport

Multi-species mass transport is solved using the equations from Chapter 1 1.11 and 1.12 for diffusive mass transport and 1.5 and 1.21 for the momentum induced convective transport . Maxwell-Stefan the most detailed diffusion model is employed for the study of chapter 3 where the geometry is simpler, and diffusion is the primary form of transport. The mixture-averaged diffusion model is used in the study of chapter 4 where channel geometry is more complex and induces convective mass transport.

2.4.2 Electrochemistry

The dependent variables for the electrochemistry equation are electrolyte potential ϕ_l and electric potential ϕ_s. They are obtained by solving the governing equations for conservation of charge and Ohm's law described as the following:

$$\nabla \cdot (-\sigma \nabla \phi) = i_{vol} \tag{2.1}$$

Where σ is the conductivity and i_{vol} is the volumetric current source term ($\mathrm{A\,m^{-3}}$) which is obtained from the product of active specific surface area ($\mathrm{m^{-2}}$) and local current density ($\mathrm{A\,m^{-2}}$). The local current density for hydrogen oxidation and oxygen reduction reactions can be modeled by Butler-Volmer equation 2.2, and the Tafel equation 2.3 approximations respectively.

$$i_a = rf \times i^0_{CL_a} \times \left(\frac{C_{H_2}}{C_{H_{2,ref}}}\right)^{0.5} \times \left(\frac{(\alpha_a + \alpha_c)F\eta}{RT}\right) \tag{2.2}$$

$$i_c = -rf \times i^0_{CL_c} \times \left(\frac{C_{O_2}}{C_{O_{2,ref}}}\right) \times 10^{\eta/A_c} \tag{2.3}$$

Where rf is the roughness factor, α is the charge transfer coefficient, A, is the cathodic Tafel slope, and $i^0_{CL_c}$ is the exchange current density. Concentrations of reactive gasses are determined by solving the equations of mass transport. The total overpotential can be obtained by:

$$\eta = \phi_s - \phi_l - E_{rev} \tag{2.4}$$

Where E_{rev} is the reversible potential obtained from the operating conditions. For solving the electrochemistry equations, the anode current collector is set to 0V and the cathode current collector is set to the operating cell voltage. The other boundaries are considered insulated.

The values of all necessary parameters used in the simulations of chapter 3 are listed in tables 3.2 and 3.1 and for chapter 4 in 4.2 and 4.2

Chapter 3

STUDY OF THREE FLOW FIELD DESIGNS

Studies to-date have not inspected the interaction between flowfield design and operating conditions of the three most conventional designs, parallel, single serpentine, and multiple serpentine, using both experimental and simulation methods. In this work, a comprehensive experimental study was carried out to characterize the interaction between operating conditions and flowfield design. The studied parameters included operating current density, RH, and flow rate. In addition, a finite element-based 3D isothermal steady state model was developed to compare with the experimental results for improved fundamental understanding. The advantages and disadvantages of each flow field under various operating conditions were identified, which provides a guideline for future technology development.

3.1 Experimental Methods

In this study, three flowfield channels, as shown in Figure 3.1, were designed and fabricated for experimental study. Each flowfield was machined on POCO Graphite plates, which has excellent electrical and thermal conductivity and corrosion resistance [5].

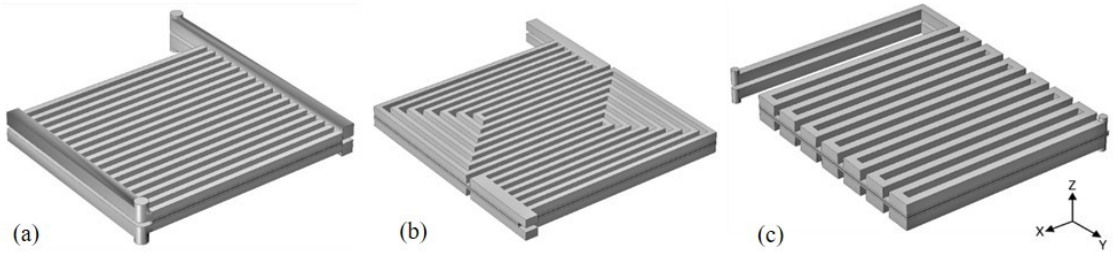

Figure 3.1: Illustrations of (a) straight parallel, (b) multiple channel serpentine, and (c) single channel serpentine flowfield designs.

The channel design parameters of each flowfield are presented in Table 3.1. The total active area was designed to be 5 cm^2 with the width and length to be 2.2

cm and 2.3 cm, respectively. Due to the difference in flow area, the order of increasing velocity and pressure drop of the design is straight parallel channel, multiple-channel serpentine, and single serpentine, under the same operating condition [13, 85]. For straight parallel and multiple channel serpentine designs, the dimension of the distribution header was designed to be $1.3\,\mathrm{mm}^2$ for reducing pressure drop in the header and enhancing uniform flow distribution in the channel.

Geometry Parameters	Straight Parallel	Multiple Serpentine	Single Serpentine
No. of channels	18	7	1
No. of passes	1	3	14
Channel width (mm)	0.610	0.533	0.787
Channel depth (mm)	0.800	0.800	1.016
Rib width (mm)	0.610	0.533	0.800
Flow area (mm^2)	8.78	2.98	0.80
Channel length (cm)	2.1	6.4	27.8

Table 3.1: Geometric parameters of the three flowfield designs

3.1.1 Protocol

All cells were broken-in and evaluated using an in-house developed benchmark testing protocol listed in Table 3.2. The break-in protocol is to activate MEA performance by cycling between open circuit voltage (OCV), 0.65 V, and 0.4 V, 12 times. Dry and wet polarization tests were done at 50% RH and 100% RH inlet gas humidification to study fuel cell performance at full load range. Then RH sweep was performed to evaluate the sensitivity of the fuel cell performance to humidity at constant current condition ($0.8\,\mathrm{A\,cm}^{-2}$). To ensure consistent start condition, the cell was purged with a high reactant flow between steps to remove condensed water. Lastly, cell performance at $0.8\,\mathrm{Acm}^{-2}$ was evaluated at four stoichiometric ratios (2/2, 5/5, 10/10, and 20/20) to study the effect of channel flow velocity on performance under both dry (40% RH) and wet (100% RH) conditions at high temperature (80°C).

Protocol	Temp.	Inlet RH	Pressure	Stoich. Ratio (An/Ca)	Load Control	Step hold time
	(C)	(%)	(kPa)			(sec)
Cyclic Voltametry	30	100	100	.02/.04 (SLPM)	1.2 - 0.1	50 mV/sec
Break-in	80	100	50	2/2	OCV, 0.65, 0.4V	120, 300, 300
Wet Polarization	80	100	100	2/2	OCV-0.2V	90
Dry Polarization	80	50	100	2/2	OCV-0.2V	90
RH Sweep	80	40-100	100	2/2	0.8A cm^{-2}	600
Stoich. Sensitivity	80	40,100	100	2/2-20/20	0.8A cm^{-2}	120

Table 3.2: Protocol and operating conditions for fuel cell testing with back pressure controlled at ambient pressure

3.2 Experimental Results and Discussion

Fuel cell performance under both wet and dry conditions, relative humidity sweep, and stoichiometry sweep were obtained using Greenlight station and Gamry Reference 3000. More than two repeated tests were performed to ensure a statistically significant trend can be observed from the results.

3.2.1 Polarization

Steady-state fuel cell polarization curves were obtained for both wet and dry operating conditions as shown in Figure 3.2. Under wet operating conditions (3.2(a)), all three cells have similar and minimal high frequency resistances due to adequate cell compression and the membrane being fully hydrated, especially at low current density regions. Performance wise, both serpentine designs perform similarly, while the straight parallel channel suffers from flooding when current density is above $0.2\,A\,cm^{-2}$. For the straight parallel channel, limiting current behavior due to oxygen depletion [86] can be observed when current density is near $0.37\,A\,cm^{-2}$. In addition, backswing behavior at low voltage due to the water dynamics and the inability of the flow field to expel liquid water in parallel channel design, which was also observed in [34, 87]. Comparing multiple and single channel serpentine, even though the general performance is similar, minor difference can be observed in the low and high current density regions. Due to its long effective channel length, the single serpentine design is expected to suffer from water accumulation near the exit of the channel as well as at the 90°bends as observed by Pekula [88]. On the other hand, the single channel serpentine shows signs of increasing HFR at high current density, which is an indication of increasing membrane resistance due to drying. This is likely due to high heat generation combined with high channel velocity in the single serpentine design, especially near the inlet region. The NR-211 membrane is very sensitive to RH and temperature and its proton transport resistance increases with increasing current density due to higher heat generation and anode

drying out caused by electro-osmotic drag in the membrane [89, 90]. With moderate pressure drop and flow distribution, the multiple-channel serpentine achieves the highest current density under wet operating conditions.

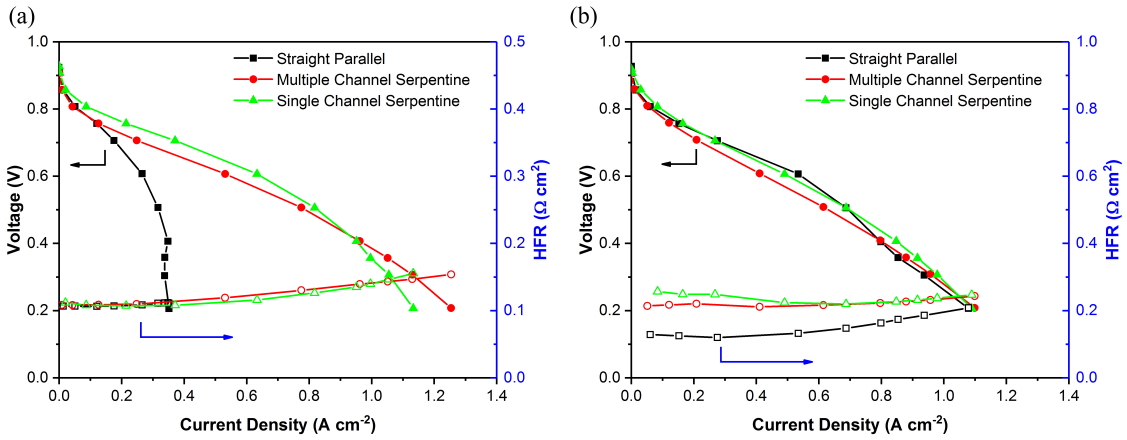

Figure 3.2: Experimental results for all three flow field designs under (a) wet operating conditions (80°C, 100% RH, and Stoic An/Ca, 2/2) and (b) dry opearting conditions (80°C; 50% RH; Stoic An/Ca, 2/2). Solid symbol: voltage; Open symbol: HFR.

Under dry conditions (3.2(b)) all three flowfield designs perform well. This indicates that no debilitating amount of liquid water condensation occurred in the cell to hinder oxygen transport. The performance and HFR results from both multiple and single channel serpentine designs are similar. On the other hand, the trends of performance and HFR from the parallel channel design show some distinct behavior. Even though there is no liquid water in the parallel channel, the membrane remains relatively well hydrated as observed from the HFR when the current density is less than $0.6\,\mathrm{A\,cm^{-2}}$ [79]. Membrane dry out can be observed when current density is greater than $0.6\,\mathrm{A\,cm^{-2}}$for the parallel channel design due to increasing heat generation and electro-osmotic drag. Consequently, the performance suffers from increasing ohmic resistance. However, the ohmic loss cannot entirely account for the sharp decrease of the performance. This indicates that the cathode may also suffer from additional mass transport loss due to increasing water content in the parallel channel design. Overall, channel design has a more significant impact on fuel cell performance under wet operating conditions and the serpentine design can more effectively remove liquid water in the channel to prevent severe flooding.

3.2.2 Relative Humidity Sweep

Since channel design is sensitive to operating RH, fuel cell performance was investigated by sweeping RH between 40 and 100% at $0.8\,\mathrm{A\,cm^{-2}}$. This protocol is a more stringent test to run under wet conditions because the cell has to sustain 10-minute load hold. The steady-state data (3.3a) show decreasing resistance and increasing performance with increasing RH, which is similar to the trends observed by Yan et al. [91]. The higher RH condition increases membrane hydration and thus reduces proton transport resistance. Upon further examination of the transient data (3.3b-d), cell voltage dropout and instability caused by water flooding can be observed for parallel and multiple channel serpentine designs [92]. While the single channel serpentine design demonstrates robust performance for all RH conditions, the straight parallel design shows signs of flooding toward the end of 60% RH condition. At 80% and 100% RH, stable performance cannot be maintained at $0.8\,\mathrm{A\,cm^{-2}}$. The single channel serpentine, however, is able to hold the load under all RH conditions with the highest performance at 100% RH. The multiple-channel serpentine design shows slight improvement and the voltage dropped out at 100% RH condition. The RH sweep protocol effectively evaluated the sensitivity of the flowfield design to channel water flooding. The peak performance of parallel and multiple channel serpentine is between 60-80% RH and 80%-100%, respectively, while the single channel serpentine can be operated stably under fully humidified conditions.

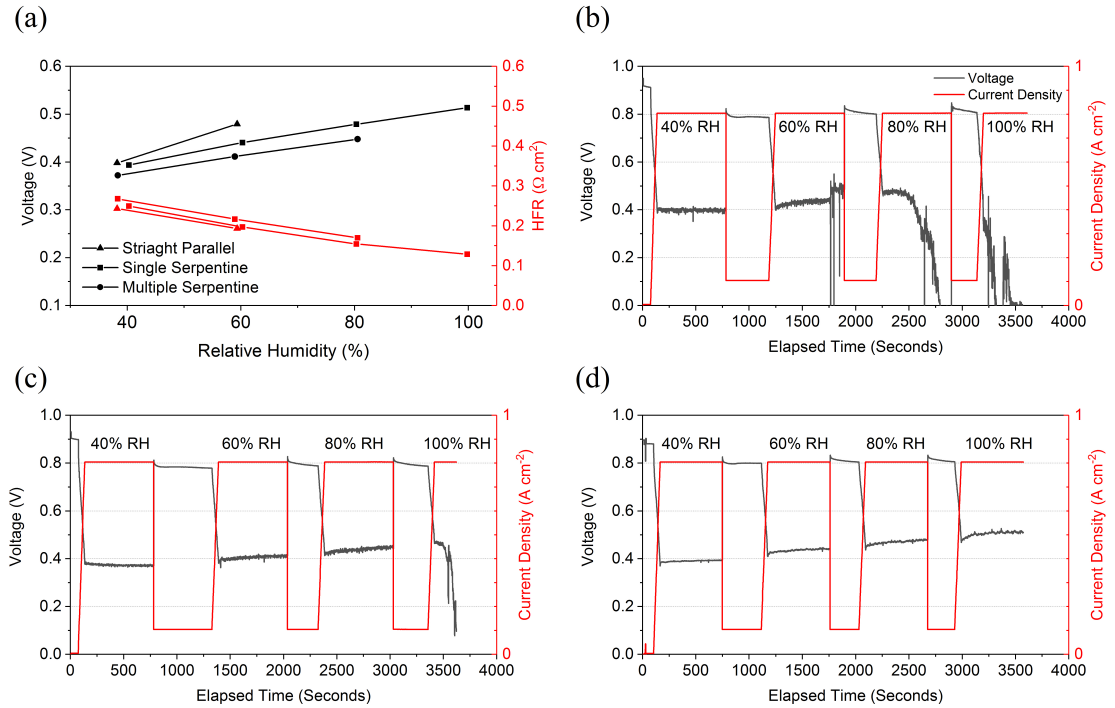

Figure 3.3: Fuel cell performance as a function of relative humidty at 80°C, 100kPa, Stoic An/Ca, 2/2 and 0.8 A cm^{-2}. (a) steady-state performance and transient performance of (b) parallel channel, (c) multiple channel serpentine, and (d) single channel serpentine.

3.2.3 Stoichiometric Sensitivity

Besides RH, fuel cell performance also depends strongly on flow stoichiometry, which determines the flow velocity and pressure drop. Therefore, stoichiometric sensitivity tests were performed under both wet and dry conditions at 0.8 A cm^{-2} and the steady-state results are shown in 3.4 and 3.5 respectively. For pressure drop measurements, the accuracy of the pressure transducer is rated to be 1.7 kPa. Therefore, the trend of the pressure drop is of interest rather than the absolute value, especially a pressure drop less than 2.5 kPa. Under wet conditions, it can be clearly observed from Figure 3.4a that the HFR increases with increasing stoichiometric flow, which demonstrates the effectiveness of removing liquid water by increasing flow rate. For all three channel designs, the lowest voltage occurred at stoichiometry of 2 due to some flooding. For the single serpentine flowfield, fuel cell performance remained similar when the stoichiometry is greater than 5. For these conditions, the

effect of reducing mass transport loss and increasing ohmic loss (HFR) nearly offset each other. The voltage of the parallel channel design increased with increasing stoichiometric flow. For this design, the improvement of mass transport loss from increasing flow rate surpass the loss from ohmic resistance. On the other hand, the multiple channel serpentine design showed an optimal performance when the stoichiometry is near 5. The ohmic loss became significant when the flow rate exceeds the stoichiometry of 5. Overall, for the wet conditions, increasing the flow rate is beneficial for preventing mass transport loss due to flooding as long as the ohmic loss and pressure drop are reasonable.

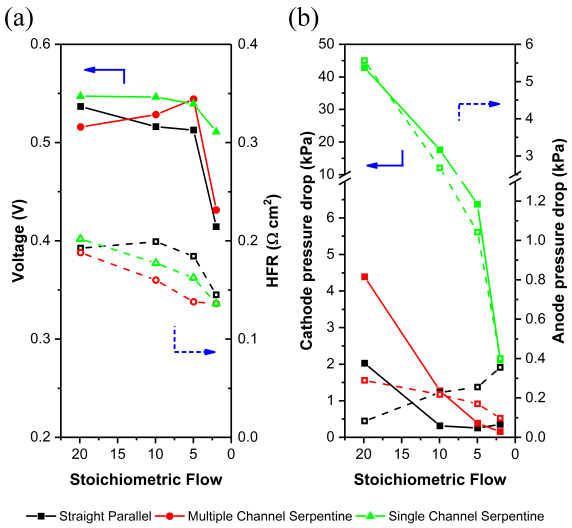

Figure 3.4: Effect of stoichiometric flow on (a) performance and (b) pressure drop at high humidity conditions (80°C; 100% RH; 100kPa vent; 0.8 A cm^{-2})

At dry conditions, the same dynamics are observed where increasing the flow rate increases the water removal and membrane dry out, subsequently leading to higher HFR. Water accumulation at the lower flow rates is also reflected by the increase of pressure drop caused by liquid water blocking the channel, an observation supported the Hsieh et al. who studied flowfield plates [93]. Although there is water present to block the reactant transport at dry conditions, the ohmic losses dominate over the mass transport losses for all cells. Decreased flow and increased water content increased the performance of at low RH.

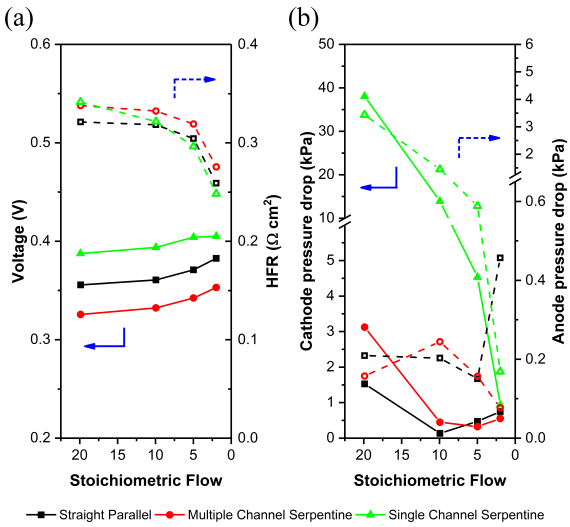

Figure 3.5: Effect of stoichiometric flow on (a) performance and (b) pressure drop at low humidity conditions (80C; 40% RH; 100kPa vent; 0.8 A cm^{-2})

Overall, increasing the flow rate is beneficial for preventing mass transport loss due to water flooding. A high stoichiometric flow may also remove too much water causing membrane dry out and lower cell ionic conductivity. The straight parallel flowfield would generally benefit from a higher flow rate due to its propensity to accumulate liquid water. The single channel serpentine design is less sensitive to the flow rate, but should be operated at a flow rate with reasonable pressure drop. It can be observed from both Figure 3.4 and 3.5 that the pressure drop of single channel serpentine design increases exponentially with increasing flow rate, which significantly increases the chance of material failure and operating cost. The multiple channel serpentine showed a greater sensitivity to the flow and RH, where a higher flow rate prevented flooding but also incurred significant additional ohmic losses.

3.3 Simulation Results

A COMSOL Multiphysics® based dry fuel cell model is developed to study the fuel cell performance of three flowfield designs under dry operating conditions

3.3.1 Comparisonn of Dry Polarization Curve

To validate the developed model, simulation results of three flowfield designs are compared with the experimental data under dry conditions in Figure 3.6. Model predictions show very good agreement with the experimental data when the current

density is below $0.6\,\mathrm{cm}^{-2}$. At higher current densities, the simulation results over-predict fuel cell performance. This deviation can be attributed to the mass transport resistance caused by water accumulation at high current density, which cannot be captured by the single phase model. The deviation at high current densities can be observed for all three flowfield designs, which indicates that liquid water exists in all cases. The overall performance under dry operating conditions for the three designs are similar, with the parallel channel performing slightly better than the single and multiple serpentine due to more uniform current distribution through the active areas. To further understand the differences between the three channel designs, RH and reactant distributions are studied by model simulation

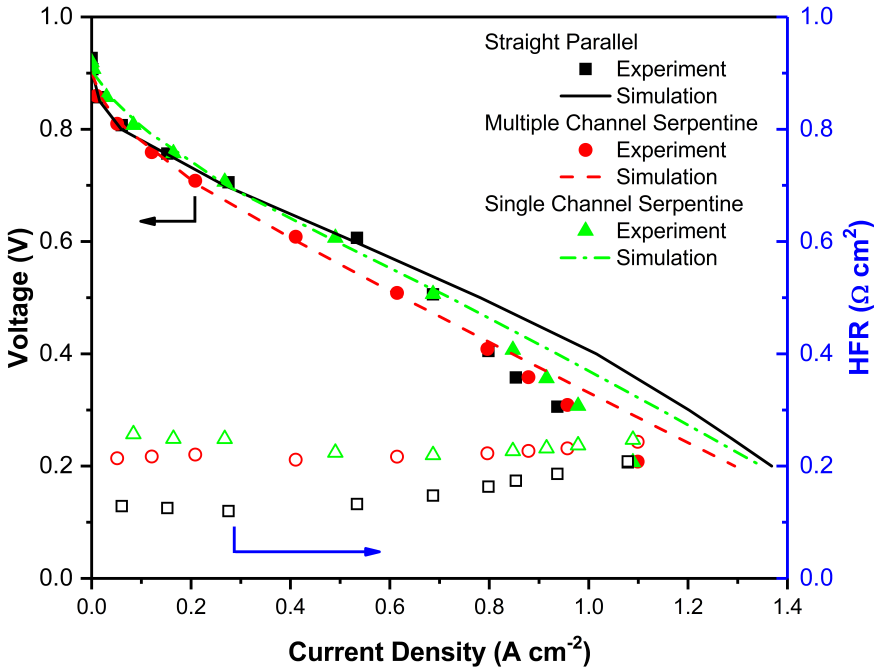

Figure 3.6: Comparison of simulation to experimental results at dry conditions (80°C; 50% RH; Stoic An/Ca, 2/2 Anode/Cathode Stoich)

3.3.2 Relative Humidity Distribution

The COMSOL model was used to simulate fuel cell performance under dry (50% RH inlet) conditions to study the RH distribution at $1\,\mathrm{cm}^{-2}$, where model prediction deviates from experimental data. The RH local distribution results at both anode and cathode catalyst layers for the three channel designs are shown in

Figure 3.7. For the anode RH distribution (3.7 d-f), drying can be observed due to increasing heat generation for all three designs. On the cathode side (3.7a-c), RH is much higher than the anode and several distinct features can be observed. Areas with RH values equal to 100% represent areas where liquid water is expected to appear, which can be observed for all three designs. This observation agrees with increasing mass transport loss at high current densities from the experimental data. In addition, higher RH levels exist under the rib region for all channel designs. This suggests that water tends to accumulate under the rib due lower gas permeation and diffusion.

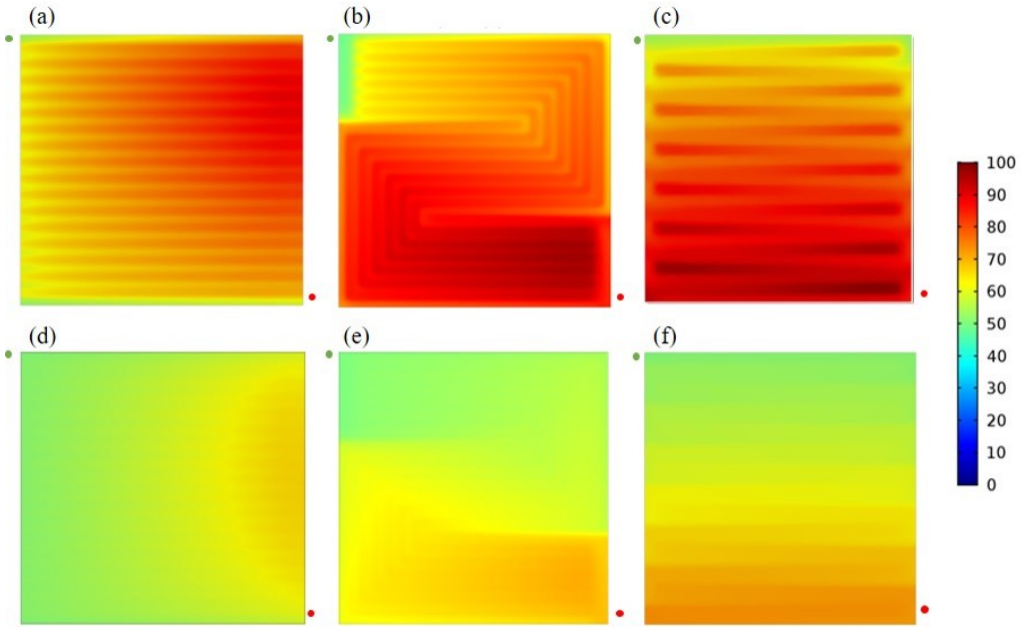

Figure 3.7: Relative humidity distribution in the cathode (a-c) and anode (d-f) catalyst layers of straight parallel (a,d), mulitiple channel serpentine (b,e), and single channel serpentine electrodes(c,f). Green dot represents inlet and red dot represents outlet.

Besides the rib/channel RH distribution, RH increases from the inlet to the exit regions due to water generation from the oxygen reduction reaction. For the parallel channel design, less RH variation was observed, which explains better model prediction. For multiple and single channel serpentine designs, RH levels are much higher near the channel exit. Due to high pressure drop for the single channel serpentine region, flow across the channel can be observed from Figure 3.7c. This cross flow is known to help remove liquid water and enhance fuel cell performance [94].

3.3.3 Reactant Distribution

A contour map of the oxygen and hydrogen partial pressure distribution at the cathode and anode catalyst layer, respectively, for an average current density of $1\,\mathrm{A\,cm^{-2}}$ are shown in Figure 3.8 Since this simulation was run at a stoichiometry of 2, the exit oxygen and hydrogen partial pressure was nearly half of the inlet concentration. In general, the oxygen and hydrogen concentrations decrease from the inlet to the exit and the oxygen concentration shows more nonuniform channel/land distribution due to its lower diffusivity. For serpentine designs, it is observed there are significant gradients before and after U-bends. For the straight parallel design, although the upper right corner appears to contrast with the lower right, there is no large gradient between neighboring channels. Additionally, the uniformity of gas distribution can be further improved by designing a larger distribution header. Overall, the parallel channel design has a much more homogenous gas concentration distribution.

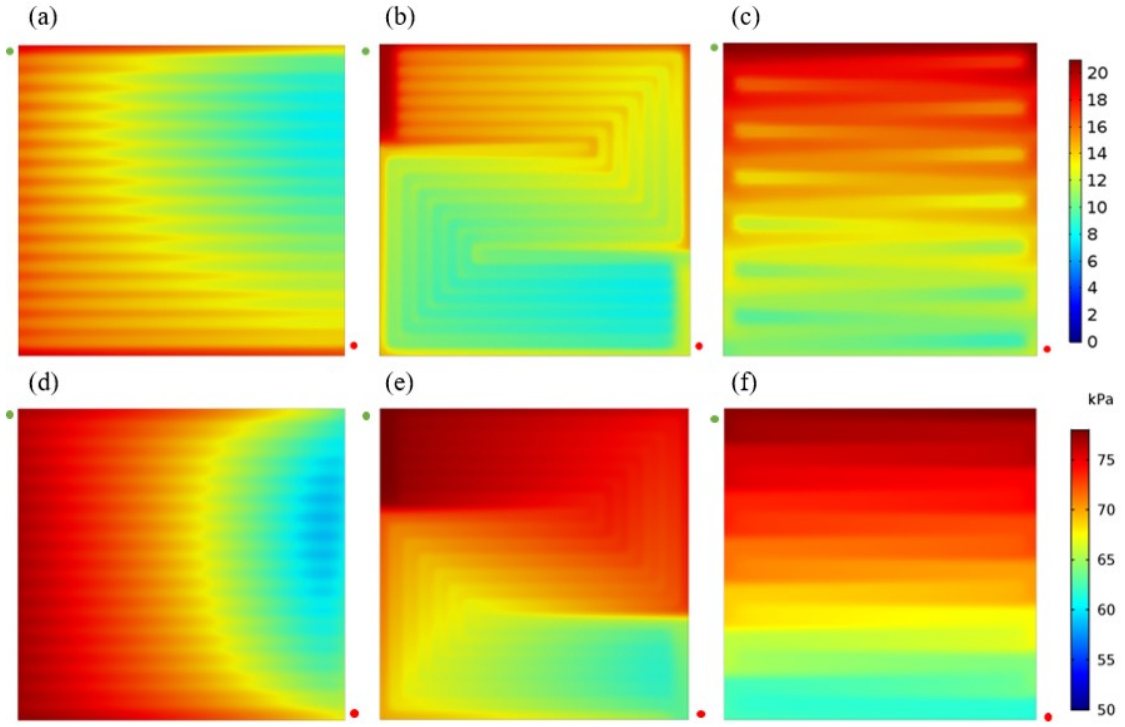

Figure 3.8: Oxygen (a-c) and hydrogen (d-f) partial pressure distribution in the catalayst layer for straight parallel (a, d), (b,e) mulitiple channel serpentine, and (c,f) single channel serpentine, green dot represents inlet and red dot represents outlet.

3.4 Summary

Three flowfield designs, straight parallel, multiple serpentine and single channel serpentine, have been studied extensively. Dry polarization results show that the three flowfields perform similarly under dry conditions and low current density. In contrast, under wet operating conditions, the parallel channel design performs poorly due to water flooding. The multiple channel serpentine design exhibits the best performance under wet conditions because of its moderate pressure drop and uniform reactant distribution. In general, increasing RH helps fuel cell performance due to the reduction of proton resistance until liquid water flooding occurs. Results show that a single channel serpentine design can remove liquid water across the RH range. Parallel and multiple channel serpentine designs can only remove liquid water effectively up to 60% and 80% RH, respectively. Dynamic results confirm that liquid flooding can cause performance to drop rapidly. To combat water accumulation, increasing flow velocity is very useful. Increasing the flow stoichiometry to above 5 can significantly enhance fuel cell performance under wet conditions. The multiple channel serpentine design shows an optimal flow rate to balance between concentration and ohmic losses. Numerical simulations using COMSOL Multiphysics® provide RH and product distribution inside each cell. The simulation results provide useful fundamental understanding and explain the experimental data qualitatively. Simulation results agree with experimental data under dry operating conditions and low current density. Discrepancies at high current density can be observed when current densities are above $0.8\,\mathrm{A\,cm^{-2}}$, which is due to increased mass transport caused by liquid water. The serpentine designs showed a higher RH near the outlets than the parallel channel, which means that RH difference across the cell increases with increasing channel length. In conclusion, operating conditions and cell design have proven to be an effective tool to manage water content and influence fuel cell performance.

Chapter 4

STUDY OF THREE FLOW CHANNEL GEOMETRIES

In all the published research, it has been shown that channel design can improve fuel cell performance and increase the concentration of reactants at the catalyst layer [95]. However, an experimental analysis of mass transport resistance using wave pattern flow channels has not been investigated. The limiting current method as developed by Baker and Caulk. has been used to measure the transport resistance in fuel cell components, GDM, micro porous layers, and catalyst layer [96–98]. The theory, however, assumes the channel is straight, square and diffusion is the major transport mechanism. The effect of varying channel design on oxygen transport resistance has not been studied before. In this study, we propose a systematic study of four parallel channel design including straight, wavy, 2D, and 3D nozzle channel to study effect of varying channel design on oxygen transport. We use for the first time the limiting current method to measure the change in the transport resistance through the porous media created by the flow field effects as well as the liquid water removal capability. The changes in transport resistance between high and low water generation regimes for four flow channel designs are studied. Further a COMSOL Mutliphysics® model is developed to study the flow characteristics in the channel and GDM domains

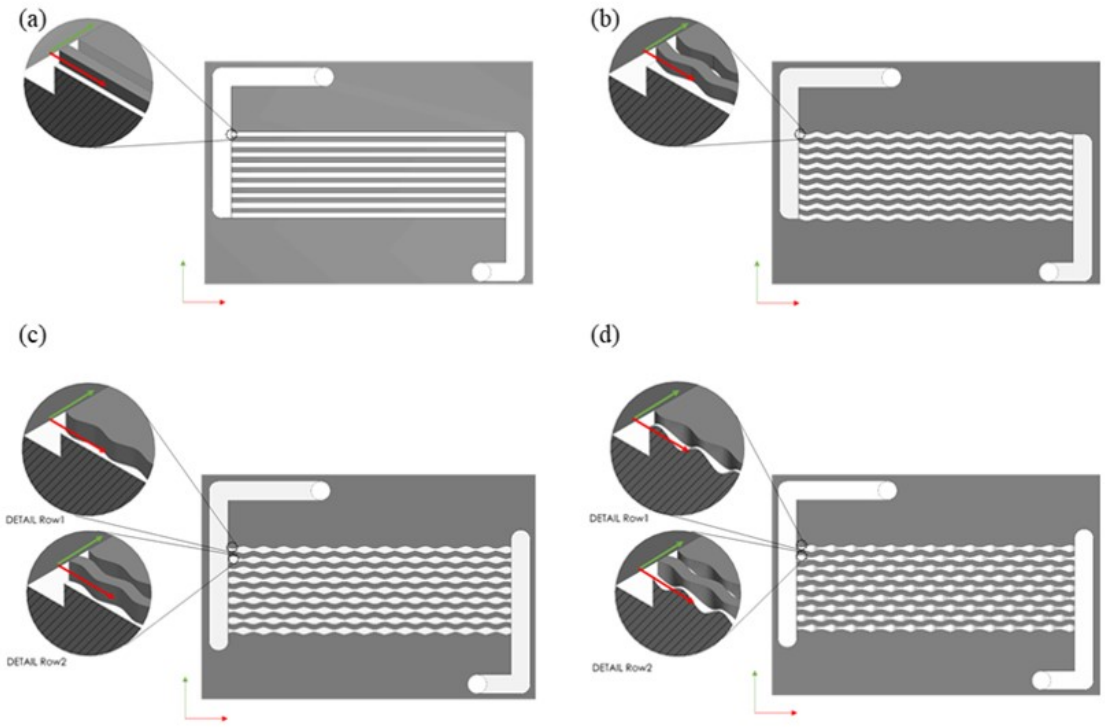

Figure 4.1: Illustration of four flow channel designs used to study oxygen transport mechanisms (a) straight, (b) wavy, (c) 2-D nozzle, (d) 3-D nozzle

4.1 Experimental Methods

The four flow channel designs used in this study are shown in Figure 4.1. The straight parallel design Figure 4.1(a) is used as a basis of comparison. Within this design, some convection occurs in the channel with diffusion driven transport through the porous media being the primary transport mechanism. The wavy design Figure 4.1(b) retains the same channel cross-sectional area as the straight parallel, however the flow path follows a sinusoidal pattern across the electrode area. As shown in simulations by Sui [44] this regularly changing direction increases the mixing of gases in the channel and reduces the channel resistance by increasing the convection into the diffusion media. Within the 2-D nozzle design Figure 4.1(c) each channel has a cycling width that alters the cross-sectional channel area. As gas flows through a constriction, or converging nozzle, it increases velocity and reduces pressure. In addition, adjacent channels are one half-cycle out of phase, so that every converging nozzle is neighboring a diverging nozzle . The aim of this 2-D nozzle design is to induce channel to channel convection between channels flowing in parallel. The 3-D nozzle design Figure 4.1(d) builds further upon the cyclic

channel dimension design by alternating the depth of the channel. This is done by increasing and decreasing depth in synchronization with increasing and decreasing width. The purpose of this design is to create forced convection through the carbon fiber (CFP), the velocity of gasses will now have a component directed towards the CFP. This increases the mass transport of oxygen to the catalyst layer. The wall locations of non-linear flow paths are drawn by the application of the sinusoidal equation:

$$y = A_w sin[\frac{\pi}{2}(\frac{4x}{\lambda} + 1)] + m_w \tag{4.1}$$

Here, A_w is the amplitude (m), λ is the pitch (m), x is the location the down the flow channel and m_w is the midline of the wave (m). Design is detailed further below (Figure 4.2).

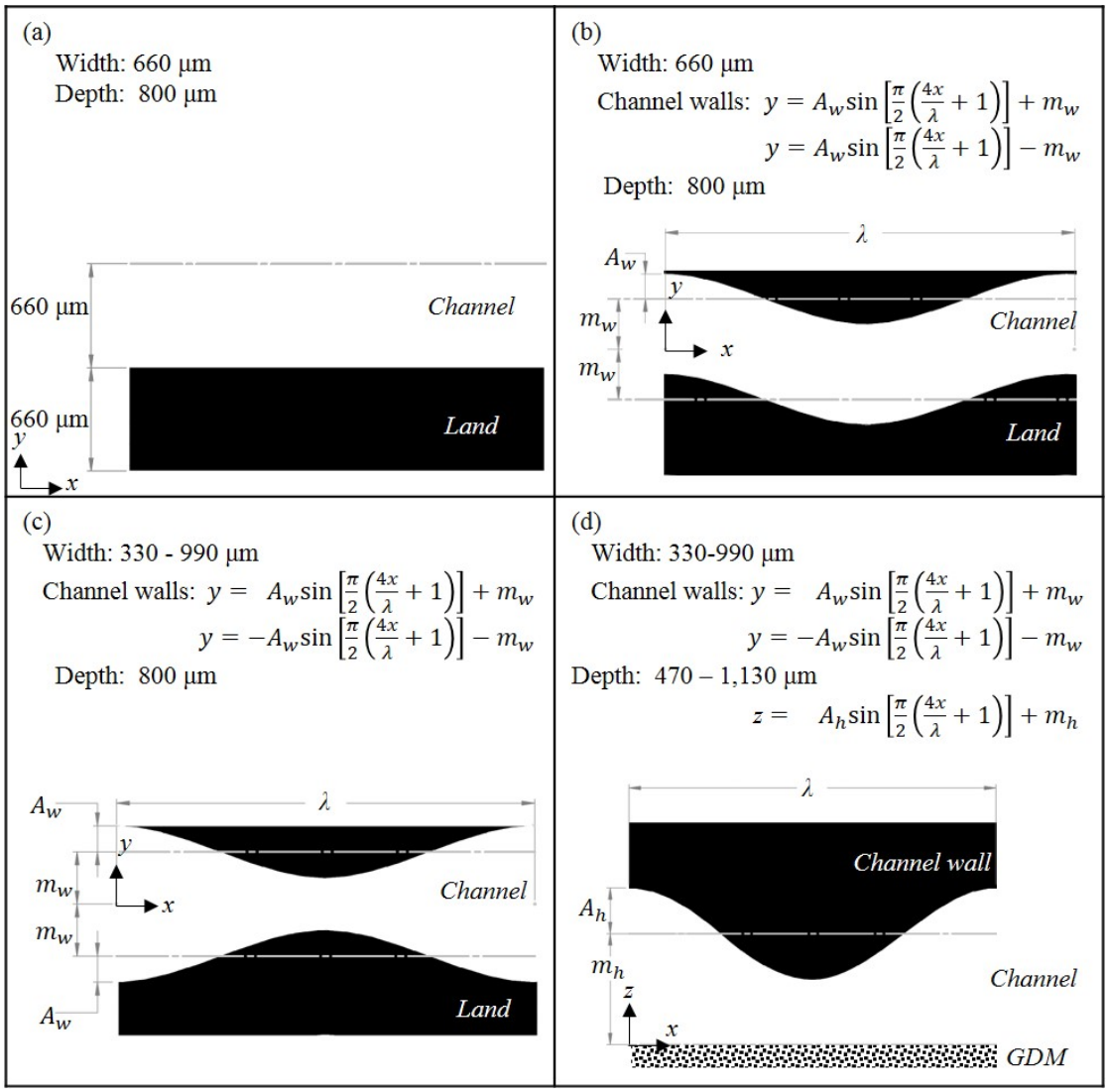

Figure 4.2: Schematics detailing channel dimension and geometries with design criteria. The profiles are drawn from dimensions of amplitude (A), pitch (λ), and the mid-line of the wave (m), x, y, z refers to the in-plane down-the-channel, in-plane cross the channel, and through-plane direction.

To improve data quality of the limiting current experiment, the flow channels must provide differential conditions i.e. maintain minimal RH, concentration, and pressure distribution across the active area [96]. This requires large flow and small active electrode area so that reactant stoichiometric ratios are at least ten at the cathode. This high flow can induce a pressure drop which can increase relative

humidity at the inlet, which can lead to condensation. Taking this into account, cells in this study all have an active electrode surface area that is masked down to 2 (m^{-2}) by use of PTFE gaskets. In all of our channel designs, the pressure drop of all tests are kept below 6 kPa, which is just above our measurement limits. This ensures that differential conditions across the active area can be achieved.

Protocol	Temp.	Inlet RH	Pressure	Flow Rate (An/Ca)	Load Control	Step hold time
	(C)	(%)	(kPa)	(SLPM)	(V)	(sec)
Cyclic Voltametry	30	100	100	.02/.04	1.2 - 0.1	50 mV/sec
Break-in	80	100	50	10/10 Stoich	OCV-0.6	900
Wet Polarization	80	100	300	0.4/2	OCV-0.3	600
Dry Polarization	80	64	100	0.4/2	OCV-0.3	600
Dry Limiting Current	80	64	300, 200, 150, 100	0.4/2	0.3-.09	130
Wet Limiting Current	70	90	300	0.4/2	0.3-0.09	130

Table 4.1: Fuel cell test protocol for flow channel geometry study

4.2 Methodology

To quantify the total oxygen transport resistance $R_{O_2}^{total}$ ($\mathrm{s\,m^{-1}}$) from the flow channel to the catalyst layer the limiting current method is used. the method based off the stoichiometric relationship between oxygen concentration and current density derived from Faraday's and Fick's law.

$$N_{O_2} = \frac{i}{4F} = \frac{C_{O_2}^{Channel} - C_{O_2}^{Catalyst}}{R_{O_2}^{total}} \tag{4.2}$$

The oxygen mole transfer rate from the channel to the electrode surface, N_{O_2} (mol $\mathrm{s^{-1}}$), is proportional to the current density, i, and is driven by the concentration gradient between the concentration at the channel $C_{O_2}^{Channel}$ $\mathrm{mol\,cm^{-3}}$. At the limiting current condition reactant is being consumed as fast as it is supplied making the $C_{O_2}^{Catalyst}$ effectively zero.

$$N_{O_2} = \frac{i_{lim}}{4F} = \frac{C_{O_2}^{Channel}}{R_{O_2}^{total}} \tag{4.3}$$

The limiting current i_{lim} (A) can be measured experimentally and $C_{O_2}^{Channel}$ can be determined from the controlled inlet conditions using the ideal gas law. Solving for the $R_{O_2}^{total}$ using equation above results in:

$$R_{O_2}^{total} = \frac{4F}{RT} \frac{X_{O_2}(p_{total} - p_{H_2O})}{i_{lim}} \tag{4.4}$$

Where X_{O_2} is the dry mole fraction of oxygen, P_{total} is the total pressure (Pa), and P_{H_2O} is the water partial pressure calculated from inlet conditions. These relations are applicable to all channel configurations.

The $R_{O_2}^{total}$ as described by Baker and Caulk is the sum resistance contributions from each component in the path of oxygen from the channel to the reaction site [99].

$$R_{O_2}^{total} = R_{O_2}^{Channel} + R_{O_2}^{GDL} + R_{O_2}^{MPL} + R_{O_2}^{electrode} \tag{4.5}$$

Channel resistance $R_{O_2}^{Channel}$ is derived from the relation of intermolecular diffusion and bulk fluid motion in the channel and the convection of reactant through the flow channel-diffusion media boundary. Gas diffusion layer resistance $R_{O_2}^{GDL}$ occurs in the pores of the CFP. The MPL resistance $R_{O_2}^{MPL}$ is controlled by Fickian and Knudsen diffusion in the micro pores ($< 0.5\mu m$) of the MPL. Electrode resistance to the flux $R_{O_2}^{electrode}$ has not yet been fully understood but arises from transport through water, ionomer, and the electrode pore structure. These resistance can be further broken down sipmly into pressure dependent $R_{O_2}^{P}$, and independent $R_{O_2}^{NP}$ contributions.

$$R_{O_2}^{total} = R_{O_2}^{p} + R_{O_2}^{NP} \tag{4.6}$$

The contribution of channel and GDL are both pressure dependent. The resistance in the MPL and catalyst structure are pressure independent processes [69].

4.3 Experimental Results and Discussion

4.3.1 Polarization Curve

Polarization curves comparing the performance of straight parallel (SP), wavy (W) 2D-nozzle(2D), and 3D-nozzle(3D) for Toray 060 DM is presented in Figure 4.3. The dry polarization is shown in Figure 4.3(a). The downward curve, indicative of concentration polarization is not observable under dry conditions,implying no condensed water is available to limit transport. Under the dry conditions the differences in the i-V curve between each flow field is negligible once the standard deviation from the three repeated tests is accounted for. There is little difference between the performance of each flow field when condensed water is not available to limit transport.

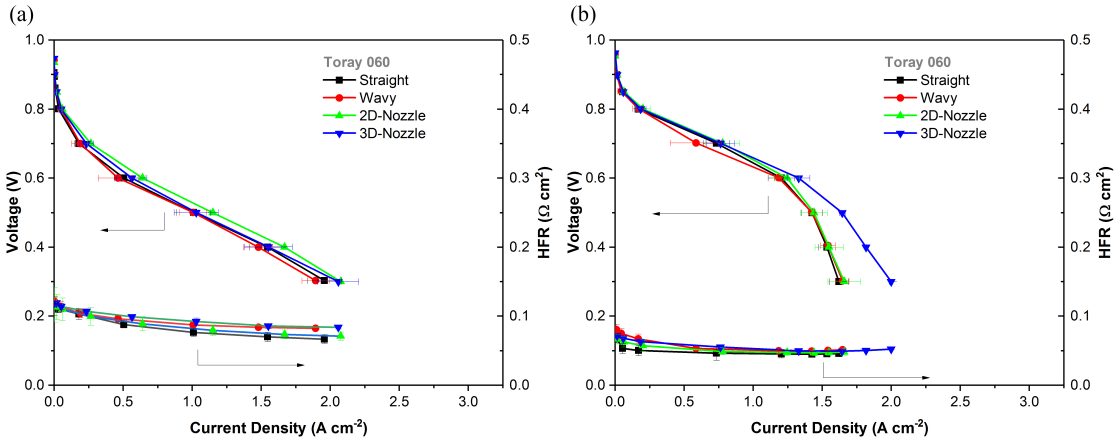

Figure 4.3: Polarization curves displaying the performance for four flow channel designs using Toray GDM at (a) dry conditions (70°C, 64%RH, 100kPa vent, 0.4/2.0 SLPM Anonde/Cathode) and (b) wet conditions (70°C, 100%RH, 300kPaabs, 0.4/2.0 SLPM Anode/Cathode

Under wet operating conditions, Figure 4.3(b), SP, W, 2D all have similar performances. HFR for all cells is at a minimum indicating optimal membrane hydration. The performance increase from improved conductivity is capped by concentration polarization as indicated by the downward curve. At the high relative humidity and current density liquid water developed in one or more of the cell components decreased the oxygen transport in this region resulting in the downward curve as limiting current is approached [100]. The clear distinction that can be observed is the performance of the 3D channel design. Above $1.25\,\mathrm{A\,cm^{-2}}$ voltage drop is less than the other designs. At 0.3V, the 3D design achieves $2.0\,\mathrm{A\,cm^{-2}}$, which is $0.4\,\mathrm{A\,cm^{-2}}$ greater than the other three designs.

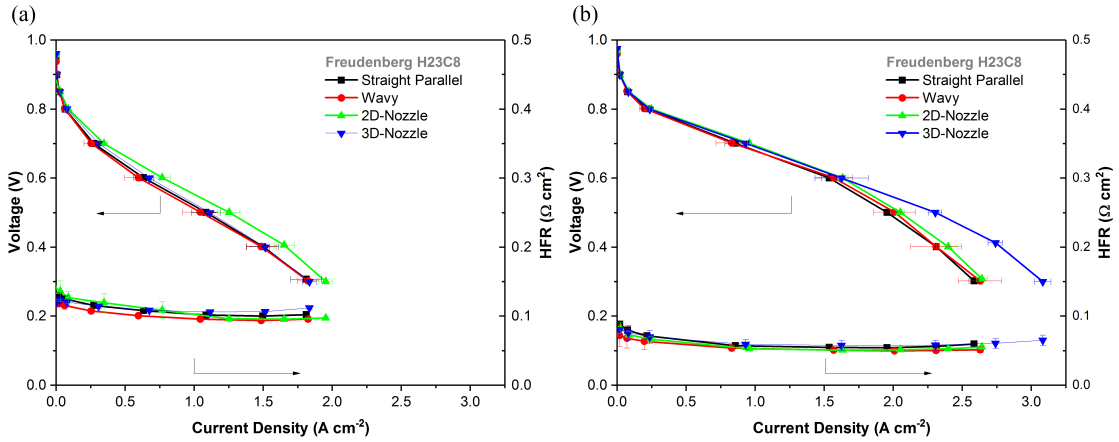

Figure 4.4: Polarization curves displaying the performance for four flow channel designs using Freudenberg GDM at (a) dry conditions (70°C, 64%RH, 100kPa vent, 0.4/2.0 SLPM Anonde/Cathode) and (b) wet conditions (70°C, 100%RH, 300kPaabs, 0.4/2.0 SLPM Anode/Cathode

Similar performance characteristics are observed using Freudenberg H23C8 GDM. The results for dry and wet polarization are displayed in Figure 4.4. Again, under low relative humidity conditions, each flow channel configuration performed equally. At 100% relative humidity,Figure 4.4, performance was significantly greater than the dry conditions and better than Toray DM performance at all tested conditions. The Freudenberg DM had greater water removal capacity, which is consistent with [101].

The 3D design distinctly outperformed the three other designs.The wavy and 2D design had little, if any, impact on transport,while the 3D clearly improved it.

4.3.2 Dry Limiting Current

The limiting current was performed as outlined in the methodology section; oxygen transport resistance vs. pressure, for three trials using Toray 060 diffusion media is plotted in Figure 4.5. Each point is derived from the slope of for the dry mole fractions at four pressures. The linear trend in Figure 4.5 indicates that the assumption of transport being pressure dependent is still relevant for the new channel designs. There was some trouble with test station pressure control for some pressure set points, resulting in a departure from the original set points in the protocol. However, the exact pressure was not required to create the profile here.

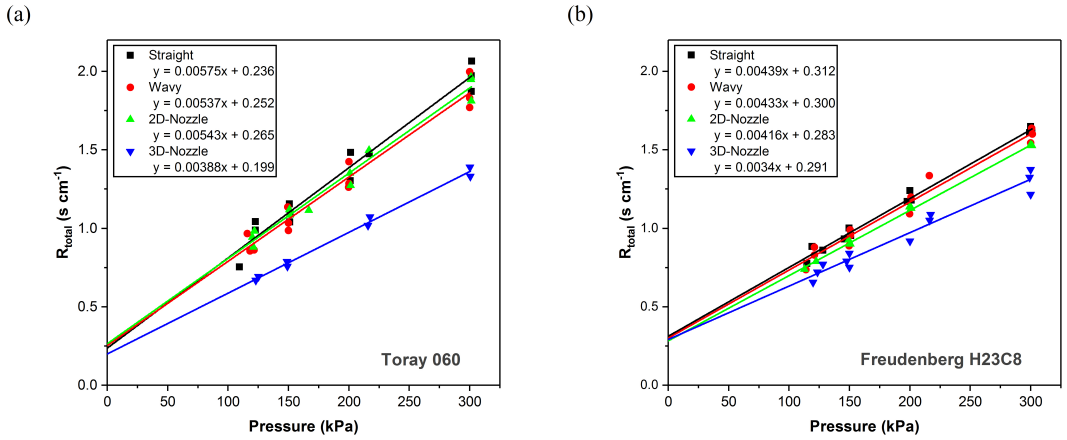

Figure 4.5: The dry transport resistance as a function of pressure for four flow channel designs using (a) Toray 060 DM and (b) Freudenberg H23C8, a total of 24 trials.

The slope of SP, W, and 2D were all relatively close to one another, indicating a minimal, non-significant change in transport resistance through the GDM. The 3D however showed a meaningful reduction in slope; convection transport was induced by channel design. The intercept of the line (pressure independent resistance) varied little, suggesting that the convective effect did not impact the MPL or electrode resistance, and is limited to the channel and/or GDM domains.

The 3D-nozzle effectively reduced transport resistance. This reduction went unnoticed in the dry polarization tests as ohmic resistance was the more significant overpotential loss at those conditions. As it was mentioned earlier, resistance is reduced. However, it is not apparent whether the reduction was in channel GDM or both. The dry transport in Freudenberg GDM for all trials is displayed in 4.5(b). Total resistance was lower than Toray but all trends for the channels still held, eliminating the conjecture of any channel-GDM dependence at the dry condition.

4.3.3 Wet Limiting Current

Results of the wet limiting current test are shown in Figure 4.6. Total transport resistance vs. limiting current are plotted. Results for 80% and 100% are excluded here to avoid cluttering the plots. The results are similar, with the difference being a shift of the curve to the left for 100% RH and to the right for 80% RH. At low voltages and high inlet mass fractions of O_2 the limiting current density can be difficult to characterize due to instability created by liquid water dynamics and peroxide evolution [78]. The limiting current used for calculation was drawn from a

line on the i-V curve that intercepted a majority of the points, neglecting swings in current density.

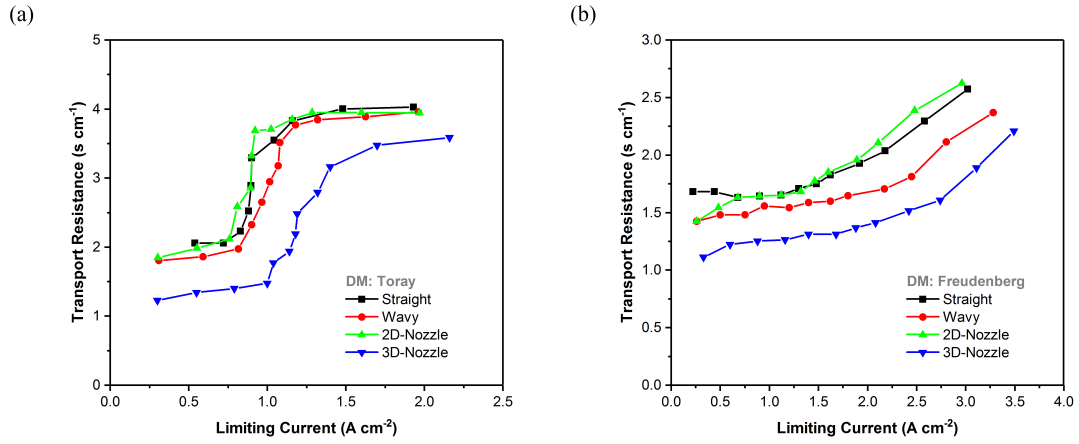

Figure 4.6: The wet transport resistance as a function of pressure for four flow channel designs using (a) Toray 060 DM and (b) Freudenberg H23C8, a total of 24 trials.

For all four channel configurations using the Toray 060 material it was observed here, as by others [102] that there exists three distinct regions to the curve, including two plateau regions that have relatively steady transport resistance for changing rates of water generation (characteristic of Toray). A wet plateau at high current density where liquid water pathways are fully developed, the cell was able to remove water without an increase in the oxygen transport resistance. Second, a saturation transition region where the line takes a steep slope, here liquid water form or break-down tendrils that enter the channel [60]. Third, a dry plateau where no liquid water was present. From Figure 4.6(a) it is observed the SP, W and 2D had near equivalent transport resistances while 3D it is reduced, the wet plateau is $0.5\,\mathrm{s\,cm^{-1}}$ lower. As the limiting current was decreased with decreased inlet oxygen concentration the 3D-Nozzle enters the transition region earlier. That is, a point at which the presence of liquid water is no longer great enough to maintain the tendrils of the wet plateau. For increasing power generation, the 3D-Nozzle is able to maintain lower water content across a larger current density range. This result can indicate a higher average water vapor saturation pressure in the GDM or that flow through the GDM is drawing the water out. In the dry plateau region, it is observed that the SP, W, and 2D all have the same dry oxygen transport resistance. The 3D design exhibits a lower dry region as was observed in the previous dry testing.

Comparing these results for Freudenberg material Figure 4.6(b). Similar behavior is observed. The Freudenberg GDM however does not have a wet plateau.

Having a lower thermal conductivity, the local heat in the porous media closer to the MPL is higher maintaining a higher saturation pressure. Thusly, water condenses closer to the channel and water tendrils do not extend the depth of the GDM [60]. This effect can explain the larger range of current density that is in the dry plateau region as water that could potentially block oxygen transport does not extend the depth of the GDM. This effect does not however, show any added benefit to channel GDM pairing.

Comparison of the four different flow channel designs reveals the 3D-nozzle design performs best, it can increase transport of oxygen under both wet and dry conditions. Considering the source of these improved transport properties it had been mentioned earlier that designs like the wavy could improve heat transfer, a temperature difference between the catalyst layer and channel could also induce convection, and a faster removal of product. However, as Zhang et al. showed in their study on this kind of transport in fuel cells, the effect in PEMFC is very small given the small temperature gradients [103]. Momentum induced convective transport is sending oxygen to the catalyst layer. Under the wet conditions the mechanism is more difficult to explain improvement. In the channel, at nozzle sections, gas velocity increases could remove liquid water through shear and drag forces. Flow in the diffusion media could move condensed water to create a path for oxygen. Alternatively, as mentioned earlier lower pressure in the expansion could draw liquid water towards the channel. To further analyze the flow characteristics a COMSOL Multiphysics model was developed.

4.4 Flow Simulation

A COMSOL Multiphysics model was constructed to simulate the gas flow on the cathode side to further study the effect of channel design. The model is applied to both the SP (baseline) and 3D (performance enhancing) design with the coupling of the Brinkman equations in porous media and transport of concentrated species interfaces.

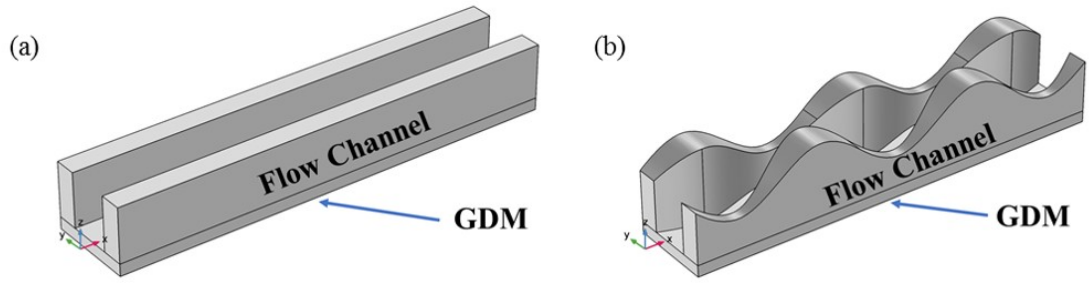

Figure 4.7: Modeling domain for a) baseline straight channel and b) 3D-nozzle flow channel.

To reduce the time required to solve the model a 0.66 cm length of channel is modeled for each design. The modeling domain is limited to the channel and GDM regions as it was discovered in experimental testing that the resistance in the MPL and CL region are not reduced using the 3D channel. The properties of the GDM region are for that of Toray 060. Since it is clearly shown the resistance is reduced in dry conditions and given the difficulty in modeling two-phase flow [81] the simulation is restricted to a single-phase isothermal model. The molar transfer rate of oxygen out, and water into the GDM domain are for a constant current density of $1\,\mathrm{A\,cm^{-2}}$. The physical parameters are listed in the table below.

Parameter	Value	Units
Temperature	80	C
Stoichiometry	10	
Current Density	1	A $\mathrm{cm^{-2}}$
Relative humidity	64	%
Dynamic viscosity	1.76 x 10^{-5}	Pa s
Porosity	0.725	
Tortuosity	0.8	
Permeability down the channel (x - axis)	12.8 x 10^{-12}	$\mathrm{m^2}$
Permeability across the channel (z - axis)	21.0 x 10^{-12}	$\mathrm{m^2}$
GDM thickness	176	μm
Channel length	0.66	cm
Electrode area	.087	$\mathrm{cm^2}$

Table 4.2: Input parameters for three dimensional flow simulation.

4.4.1 Simulation Results

The results are given in Figure 4.8 for velocity at the center of a channel in the x-y plane and Figure 4.9 for the partial pressure at four points at the center of the channel in the y-direction.

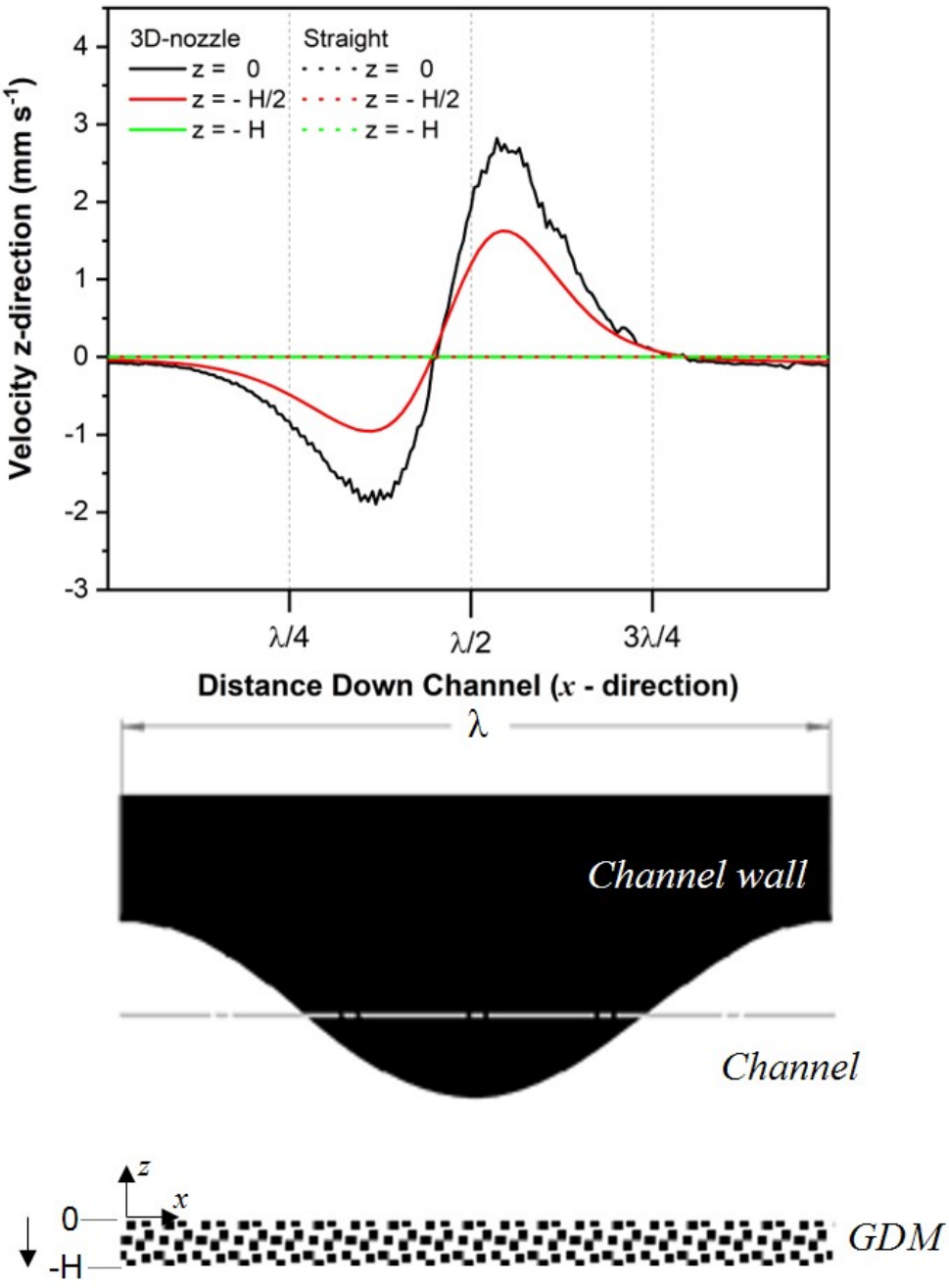

Figure 4.8: Down the channel velocity (x-direction) for the 3D-nozzle and Straight parallel designs for a single section of channel

In Figure 4.8 it is clear that the 3D-nozzle channel design induces a flow into the GDM whereas using the straight parallel design there is comparatively no flow in the z-direction. The flow created by the 3D-nozzle is regularly repeating, cycling between driving into the into and out of the GDM. This inward flow serves to lower the measured transport resistance in the dry limiting current section. Though this simulation is carried out for conditions in which there is no liquid water it can be extrapolated from this result that this flow pattern can aid in water management when liquid is present. The flow can create enough drag force in the diffusion media that droplets condensed on GDM fibers are pushed out of the path of incoming oxygen. In the sections where the flow is moving out of the GDM the drag force would be able to push water out of GDM [104] resulting in an overall lower level of saturation and a subsequent lower resistance. This supports the hypotheses proposed in the experimental results section for wet limiting current.

Returning focus to the dry cell conditions under which the simulation was carried out, the z-direction partial pressure plot (Figure 4.9) aids in ascertaining the source of reduced ${R_{O_2}}^{Total}$. The partial pressure is taken along four cut-lines through the DM along the pitch of a 3D nozzle section and is plotted. These cut-lines are the converging nozzle section, diverging nozzle section, and the two mid-line points in between.

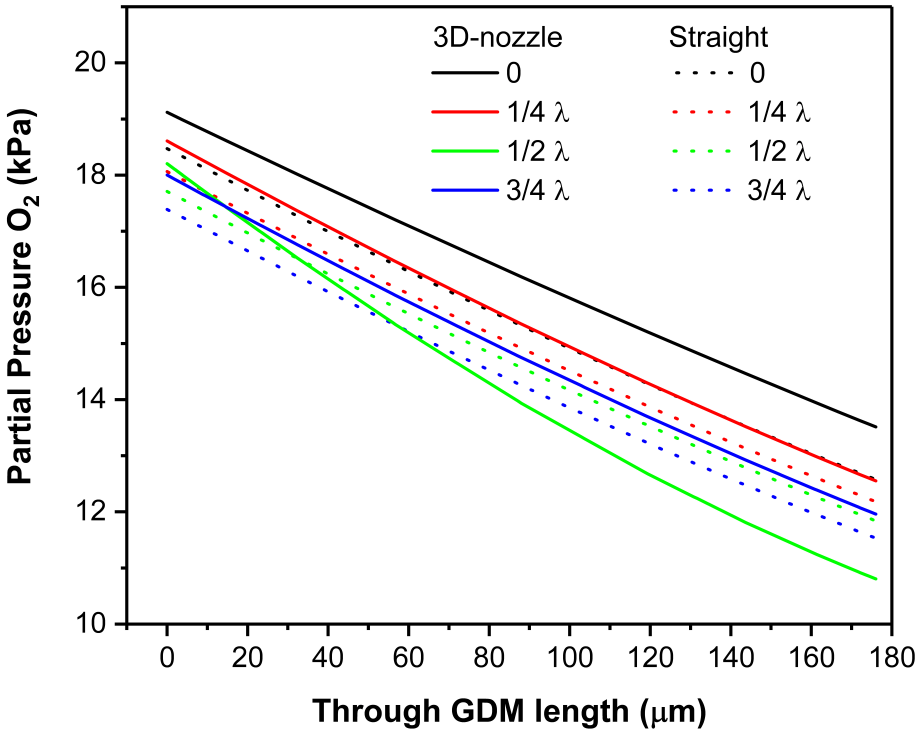

Figure 4.9: Oxygen partial pressure through the depth of the GDM at four locations down the channel.

Comparing the two flow fields the 3D-nozzle has higher oxygen partial pressure at the channel-GDM interface than the straight parallel at all points and a non-linear partial pressure profile. The expected result of the convection driven transport in the diffusion media was be the appearance of two different slopes, a largely momenta driven slope and a diffusion driven slope. This is observed to some extent as the partial pressure profiles for the 3D design are not completely linear. The concentration at the channel-GDM interface is higher and as the gasses travel into the GDM the momenta is dissipated, and diffusion becomes the primary mode of transport. In Figure 4.9 the slope of partial pressure for all lines are equal after 120 μm into the gas diffusion media, at that depth the impinging flow is no longer significant compared to the concentration gradient. This does not however apply to the $1/2\lambda$ profile. As was observed from the velocity profile flow is moving upward here creating a retraction effect in the GDM and lowering the concentration. From the simulations it is clear there is induced flows in the GDM that impacts the

concentration.

4.5 Summary

From the limiting current experiments conducted, the wavy and 2D-nozzle channel designs have little effect on the transport resistance. The 3D-nozzle design did however reduce transport resistance under both wet and dry conditions. To better understand this phenomenon a section the 3D-nozzle was simulated using COMSOL Mulitphysics®, a section of the straight parallel channel was also modeled for comparison. From these results it was understood that the 3D-nozzle induced a flow into the GDM towards the catalyst layer. This flow reduced the channel-GDM transport resistance significantly and the diffusion media resistance marginally. The flow present in the diffusion media, although not enough to substantially increase the performance at the dry conditions, may be the source of significantly reduced wet transport resistance when liquid water was present. The flow removed water by shear and drag forces. The 3D-nozzle flow field enhances oxygen transport under both wet and dry fuel cell operating conditions and can be further investigated for its positive performance for water removal capability.

Chapter 5

CONCLUSION AND FUTURE WORKS

This research focused on the experimental and compuational study of flow field designs and gas diffusion media in PEM fuel cells. We began by examining three common flow field distribution patterns and the effect on operating conditions on performance. We then focused our study on the channel, we examined transport resistance for three channel geometries. Finally, given the results of our experiments on channel design, we concentrated our investigation on the source of reduced transport resistance with the 3D-nozzle design.

From the first study of three flow fields the parallel channel showed a great propensity for flooding with water if it was operated at above 60% RH. This could however be countered with high flow rates. From the simulation results the parallel channel design produced the greatest homogeneity in reactant and product distribution giving value to the use of this design. The single channel serpentine showed better performance at most operating conditions but produced a large pressure drop during the experiments and showed least homogeneity of species concentration in the simulations. Best use of the design is kept to small lab cells that operate under a large array of conditions. The multiple channel serpentine provided trade-offs between the two other designs. In testing it was operated at 80% RH without flooding and did not have excessive pressure drop even at the higher flow rates.

In our second study of channel design we examined the oxygen transport resistance of three channel geometries using the limiting current method. Our results showed that varying the direction of flow path parallel to the gas diffusion media, using our wavy and 2D-nozzle design, did little to enhance convective transport over the regular straight channel. This observation held for both of our tested diffusion media. The 3D-nozzle with sinusoidally changing channel depth and width significantly enhanced transport and was more capable of removing water from our wet limiting current results. It consistently had the lowest transport resistance across the whole range of water generation i.e. current density. Our flow simulation using the 3D-nozzle showed this was due to the momenta directed into and out of the porous diffusion media. Oxygen mass transport was enhanced, and water was dragged out of the gas diffusion media.

Future work will continue investigations of the 3D-nozzle design. Neutron radiography experiments can identify liquid water thickness and location and would

further enhance our understanding of how the 3D-nozzle removes liquid water. Simulations can be modified and improved two-phase model to capture flooding phenomenon. The 3D-nozzle design here featured a sinusoidally changing depth and width but could also follow a slightly different pattern, changing the length of the converging nozzle section or of the expansion section is also possible. As has been presented here the flow channel design can improve fuel cell performance via convective transport design.

APPENDIX A

A.1 Electrochemical Impedance Spectroscopy (EIS)

EIS is a in situ diagnostic tool used in PEMFC studies to do the following: 1) allow modeling of the system with an appropriate equivalent circuit; 2) differentiate the individual contribution of each fuel cell component, such as the membrane and GDM to fuel cell performance; 3) identify individual contribution to the total impedance from different electrode processes such as interfacial charge transfer and mass transport [105]. The method consists of using a potentiostat/galvanostat to impose an AC perturbation on top of the DC load from the load bank and measuring the impedance response. As the frequency of the AC perturbation is swept across a set range different time rate dependent electrochemical processes are induced. The requirement for effective measurements using EIS is that the AC signal must be low to ensure the response is linear. Perturbation is then a result of a shift from one steady shift to another steady state. This translates to a perturbation that is usually 5% of the load [106]. For analysis the frequency response of is translated into a complex impedance and plotted on a nyquist plot as shown in A.1 The high frequency range starts from the left of the plot here fast charge transport processes can be measured. In the midrange an arc is observed the radius of which corresponds to interfacial charge transfer and reaction kinetics. The low frequency region on the right corresponds to a combination of kinetics and slower diffusion processes that occur [107].

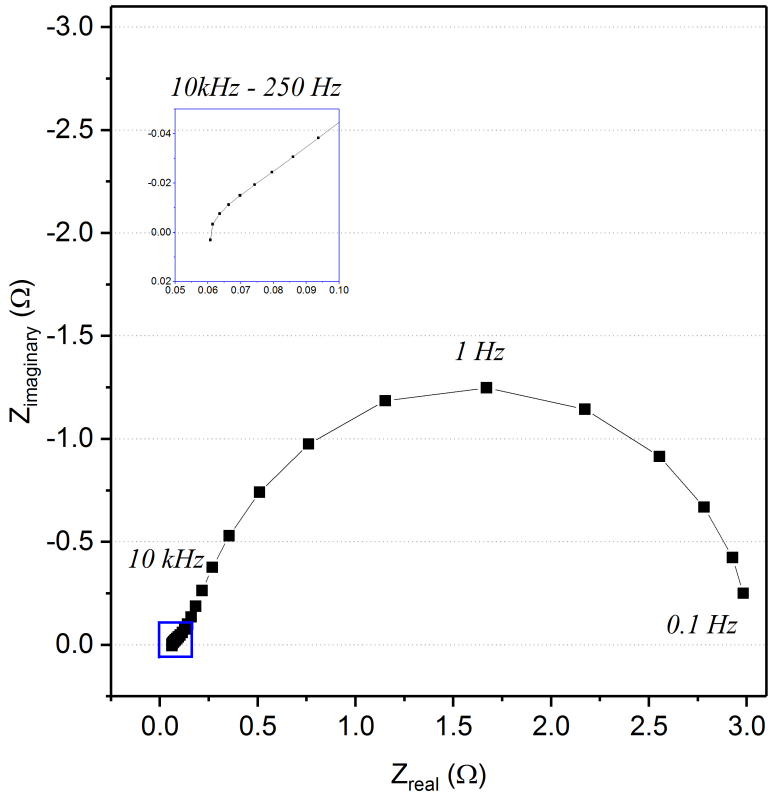

Figure A.1: Typical EIS curve, frequency range 10kHz to 0.1 Hz.

For our purposes our primary interest is the high frequency intercept with the real axis. The intercept represents the total ohmic resistance of the cell, the sum of contributions from the membrane, CL, GDM, flowfield, current collector plates and their contact resistances [108].

A.2 Cyclic Voltammetry (CV)

CV is used in this study to measure the electrochemically active surface area (ECSA) through hydrogen desorption/adsorption.The details of the process is described by Carter et al. in reference [109]. In our study hydrogen gas is fed onto the anode which serves as the reference electrode and nitrogen is fed onto the cathode. The Gamry potentiostat sweeps voltage back and forth from 0.1 to 1.2V. Hydrogen that has crossed over adsorps onto the available platinum catalyst in the

0.1 to 0.4V range and is identified as the region between the double layer capacitance region and the hydrogen adsorption peak. The area of this region corresponds to the total charge of hydrogen on platinum and is related to the ECSA by the following equation:

$$ECSA = \frac{q_{adsorption}}{\Gamma L_{pt}} \tag{A.1}$$

Where $q_{adsorption}$ ($\mathrm{C\,cm^{-2}_{MEA}}$) is the area of the curve, L_{Pt} (g $\mathrm{cm^{-2}}$) is the electrode platinum loading, and Γ is the charge required to reduce a monolayer of protons on Pt and is equal to 210 μC $\mathrm{cm^{-2}}$.

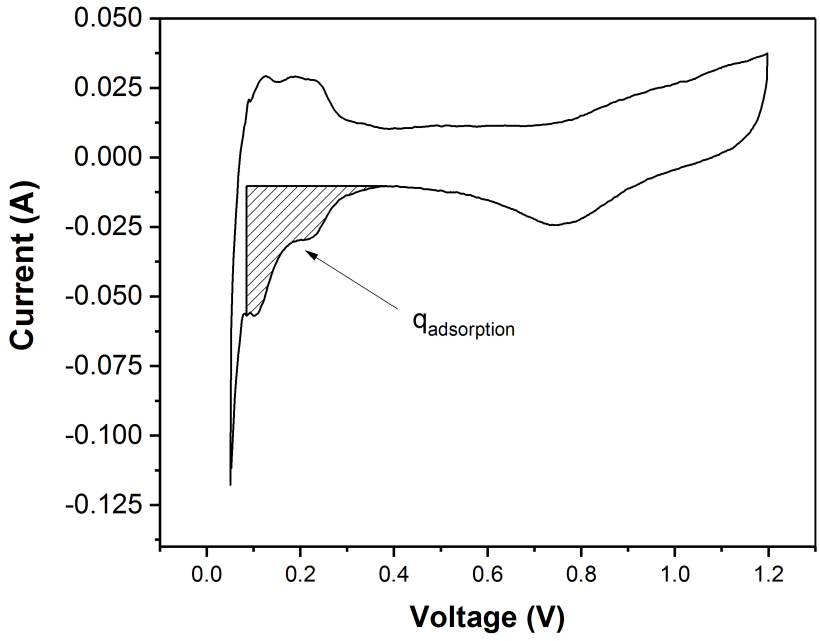

Figure A.2: Typical CV curve for PEMFC

The graph above will shift upward if crossover is present or slope if there is shorting. This is corrected for by determining the shift or slope of the double layer capacitance region which is must be horizontal and centered about zero current.

A.3 GDM Properties

GDM	Thickness (uncompressed)	Density	Air Permeability	Through Plane Resistance	Tensile Strength	Flexural Modulus	Porosity (uncompressed)
	(μm)	(g m^{-2})	m^2	(m$\Omega$$cm^2$)	(N cm^{-1})	(MPa)	%
Freudenberg H23C8	230	-	-	8 @ 1 MPa	16	-	-
Toray 060	190	0.44	12.8 x 10^{-12}	80 mΩ cm	70	40	78
Sigracet 29BC	235	-	6 x 10^{-12}	9.5 @ 1 MPa	-	-	41

Table A.1: Manufacturer and vendor specifications for gas diffusion media [110–112]

A.4 COMSOL Modeling

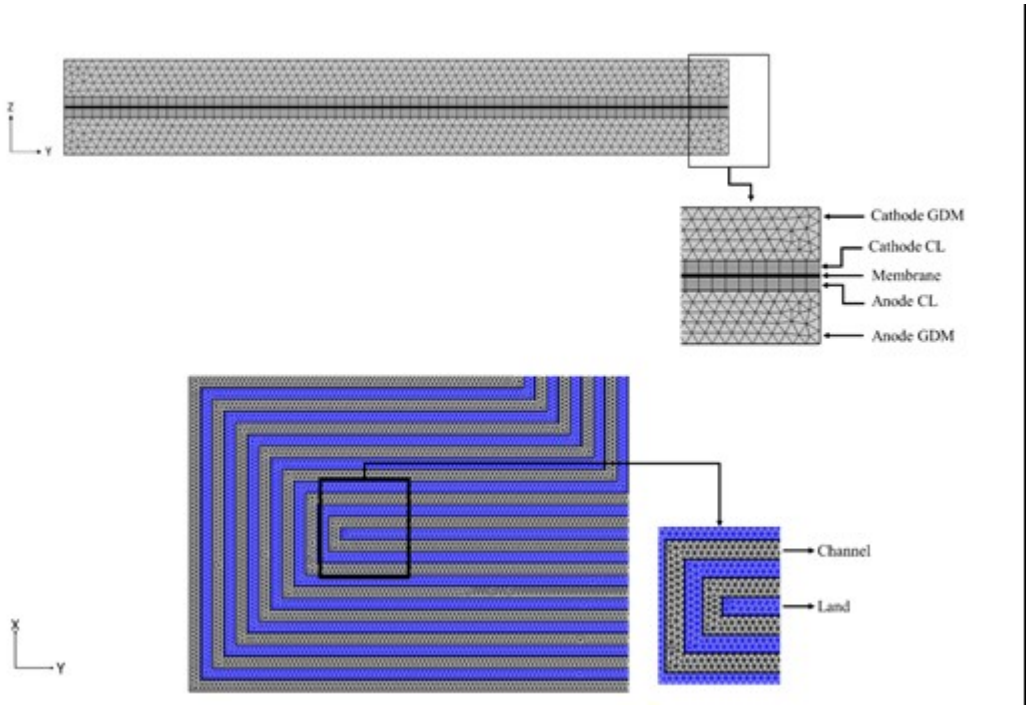

Figure A.3: Illustration of mesh structure in flow channel, gas diffusion media catalyst layer and membrane as viewed from the in-plane direction (top) and the through-plane direction (bottom).

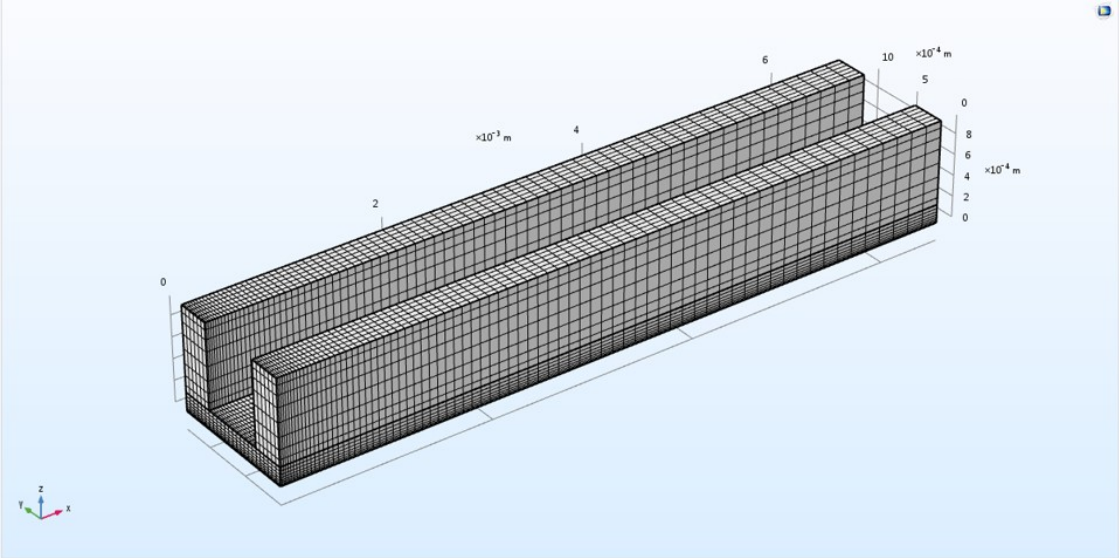

Figure A.4: COMSOL output showing mesh for straight parallel channel flow simulation.

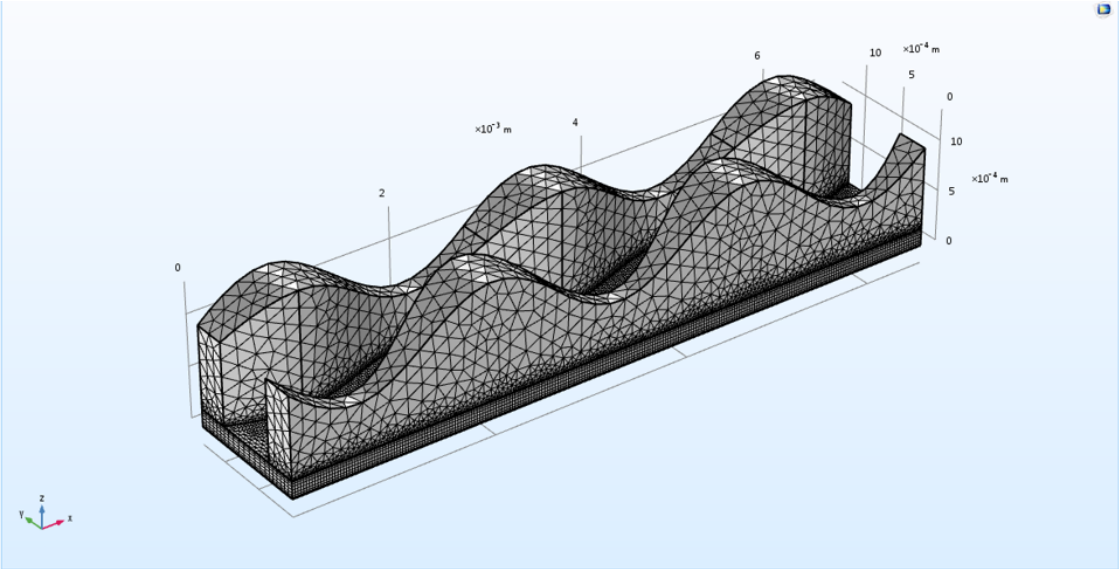

Figure A.5: COMSOL output showing mesh for 3D-nozzle flow simulation.

Input	Value
Temperature (K)	353
Pressure (kPa, abs)	100
Reversible cell voltage (V)	1.185
Kinetic Properties	
HOR Exchange current density ($A\,cm^{-2}$)	0.3
ORR Exchange current density ($A\,cm^{-2}$)	2.47
Cathodic Tafel Slope, ($mV\ dec^{-1}$)	-70
Roughness factor, rf [from experimental results]	280
Active specific surface area, (m^{-1})	5
Geometric Properties	
GDL thickness (m)	200
Catalyst layer thickness (m)	15
Membrane thickness (m)	30
Transport Properties	
Porosity of GDL,	0.4
Permeability of GDL, (m^2)	6.00×10^{-12}
Porosity of Catalyst Layer,	0.3
Permeability of Catalyst Layer, (m^2)	1.20×10^{-12}
Diffusivity of H2 in N2, at 353K ($m^2\,s^{-1}$)	1.181
Diffusivity of H2O in N2, at 353K ($m^2\,s^{-1}$)	0.355
Diffusivity of O2 in N2, at 353K ($m^2\,s^{-1}$)	0.279
Diffusivity of O2 in H2O, at 353K ($m^2\,s^{-1}$)	0.355
Anode inlet H2 mass fraction	0.743
Anode inlet H2O mass fraction	0.257
Cathode Inlet O2 mass fraction	0.241
Cathode Inlet H2O mass fraction	0.151
Cathode Inlet N2 mass fraction	0.608
Anode Viscosity at 353K (Pa s)	10.9×10^{-6}
Cathode Viscosity at 353K (Pa s)	17.6×10^{-6}

Table A.2: Input parameters for the, single phase, COMSOL simulation of three flow field designs.

Parameter	Value
Temperature (°C)	80
Stoichiometry	10
Current density ($A\,cm^{-2}$)	1
Relative humidity (%)	64
Dynamic viscosity (Pa s)	17.6×10^{-6}
Porosity	0.725
Permeability down the channel (x-axis) (m^2)	12.8×10^{-12}
Permeability across the channel (z-axis) (m^2)	21.0×10^{-12}
GDM thickness (μm)	176
Channel length (cm)	0.66
Tortuosity	0.8
Electrode Area (cm^2)	0.087

Table A.3: Input parameters for the, single phase, COMSOL simulation of flow characteristics for straight and 3D-nozzle flow channel designs.

Bibliography

[1] Alhussein Albarbar Mohmad Alrweq. *Proton Exchange Membrane Fuel Cells Design, Modelling and Performance Assessment Techniques*. Springer International Publishing AG 2018, 2018. ISBN: 978-3-319-70727-3. DOI: https://doi.org/10.1007/978-3-319-70727-3.

[2] Yun Wang et al. "A review of polymer electrolyte membrane fuel cells: Technology, applications, and needs on fundamental research". In: *Applied energy* 88.4 (2011), pp. 981–1007.

[3] Toshihiko Yoshida and Koichi Kojima. "Toyota MIRAI Fuel Cell Vehicle and Progress Toward a Future Hydrogen Society". In: *The Electrochemical Society Interface* 24.2 (2015), pp. 45–49. DOI: 10.1149/2.F03152if. eprint: http://interface.ecsdl.org/content/24/2/45.full.pdf+html.

[4] Alin C Fărcaş and Petru Dobra. "Adaptive control of membrane conductivity of PEM fuel cell". In: *Procedia Technology* 12 (2014), pp. 42–49.

[5] Allen Hermann, Tapas Chaudhuri, and Priscila Spagnol. "Bipolar plates for PEM fuel cells: A review". In: *International Journal of Hydrogen Energy* 30.12 (2005), pp. 1297–1302. ISSN: 03603199. DOI: 10.1016/j.ijhydene.2005.04.016.

[6] Dewan Hasan Ahmed and Hyung Jin Sung. "Effects of channel geometrical configuration and shoulder width on PEMFC performance at high current density". In: *Journal of Power Sources* 162.1 (2006), pp. 327–339. ISSN: 03787753. DOI: 10.1016/j.jpowsour.2006.06.083.

[7] J. Scholta et al. "Investigation on the influence of channel geometries on PEMFC performance". In: *Journal of Power Sources* 155.1 (2006), pp. 66–71. ISSN: 03787753. DOI: 10.1016/j.jpowsour.2005.05.099.

[8] Chao Wang et al. "The Experimental Measurement of Local and Bulk Oxygen Transport Resistances in the Catalyst Layer of Proton Exchange Membrane Fuel Cells". In: *The Journal of Physical Chemistry Letters* 5852.1 (2017), acs.jpclett.7b02580. ISSN: 1948-7185. DOI: 10.1021/acs.jpclett.7b02580.

[9] Nuttapol Limjeerajarus and Patcharawat Charoen-Amornkitt. "Effect of different flow field designs and number of channels on performance of a small PEFC". In: *International Journal of Hydrogen Energy* 40.22 (2015), pp. 7144–7158. ISSN: 03603199. DOI: 10.1016/j.ijhydene.2015.04.007.

[10] James Larminie and Andrew Dicks. *Fuel Cell Systems Explained*. 2nd. West Sussex, England: John Wiley & Sons Ltd., 2013. ISBN: 0-470-84857-X.

[11] A. P. Manso et al. "Influence of geometric parameters of the flow fields on the performance of a PEM fuel cell. A review". In: *International Journal of Hydrogen Energy* 37.20 (2012), pp. 15256–15287. ISSN: 03603199. DOI: 10.1016/j.ijhydene.2012.07.076.

[12] Roshanzamir et Al. *Convective Flow Field for Fuel Cell Stack*. 2017.

[13] Xianguo Li and Imran Sabir. "Review of bipolar plates in PEM fuel cells: Flow-field designs". In: *International Journal of Hydrogen Energy* 30.4 (2005), pp. 359–371. ISSN: 03603199. DOI: 10.1016/j.ijhydene.2004.09.019.

[14] Emerson R. Gallagher Peter R. Gibb Neil V. Davis. *Flow Field Plate Assembly for an Electrochemical Fuel Cell*. 2004. DOI: 10.1126/science.Liquids.

[15] Roshandel et al. "Simulation of an innovative flow-field design based on a bio inspired pattern for PEM fuel cells". In: *Renewable Energy* 41 (May 2012), pp. 86–95. ISSN: 09601481. DOI: 10.1016/j.renene.2011.10.008.

[16] Mohammad Sajid Hossain, Bahman Shabani, and Chi Pok Cheung. "Enhanced gas flow uniformity across parallel channel cathode flow field of Proton Exchange Membrane fuel cells". In: *International Journal of Hydrogen Energy* 42.8 (2017), pp. 5272–5283. ISSN: 03603199. DOI: 10.1016/j.ijhydene.2016.11.042.

[17] Shou Shing Hsieh, Sheng Huang Yang, and Chih Lun Feng. "Characterization of the operational parameters of a H2/air micro PEMFC with different flow fields by impedance spectroscopy". In: *Journal of Power Sources* 162.1 (2006), pp. 262–270. ISSN: 03787753. DOI: 10.1016/j.jpowsour.2006.06.070.

[18] Ibrahim Alaefour et al. "The role of flow-field layout on the conditioning of a proton exchange membrane fuel cell". In: *Fuel* 230 (2018), pp. 98–103. ISSN: 00162361. DOI: 10.1016/j.fuel.2018.05.062.

[19] Andrew Higier and Hongtan Liu. "Optimization of PEM fuel cell flow field via local current density measurement". In: *International Journal of Hydrogen Energy* 35.5 (2010), pp. 2144–2150. ISSN: 03603199. DOI: 10.1016/j.ijhydene.2009.12.116.

[20] David L Wood III, Jung S Yi, and Trung V Nguyen. "Effect of direct liquid water injection and interdigitated flow field on the performance of proton exchange membrane fuel cells". In: *Electrochimica Acta* 43.24 (1998), pp. 3795–3809. ISSN: 0013-4686. DOI: 10.1016/S0013-4686(98)00139-X.

[21] D H Jeon et al. "The effect of serpentine flow-field designs on PEM fuel cell performance". In: *International Journal of Hydrogen Energy* 33 (2008), pp. 1052–1066. DOI: 10.1016/j.ijhydene.2007.11.015.

[22] A Kazim, H T Liu, and P Forges. "Modelling of performance of PEM fuel cells with conventional and interdigitated flow-fields". In: *Journal of Applied Electrochemistry* (1999), pp. 1409–1416. ISSN: 0021891X. DOI: 10.1023/a:1003867012551.

[23] Phong Thanh Nguyen, Torsten Berning, and Ned Djilali. "Computational model of a PEM fuel cell with serpentine gas flow channels". In: *Journal of Power Sources* 130.1-2 (May 2004), pp. 149–157. ISSN: 03787753. DOI: 10.1016/j.jpowsour.2003.12.027.

[24] Chrysovalantou Ziogou et al. "Modeling, simulation and experimental validation of a PEM fuel cell system". In: *Computers and Chemical Engineering* 35.9 (2011), pp. 1886–1900. ISSN: 00981354. DOI: 10.1016/j.compchemeng.2011.03.013.

[25] Ryan O'Hayre et al. *Fuel Cell Fundamentals*. New Jersey: John Wiley & Sons, 2009. ISBN: 978-0-470-25843-9.

[26] Junye Wang. "Theory and practice of flow field designs for fuel cell scaling-up: A critical review". In: *Applied Energy* 157 (2015), pp. 640–663. ISSN: 18729118. DOI: 10.1016/j.apenergy.2015.01.032.

[27] Hong Liu et al. "Experimental Study and Comparison of Various Designs of Gas Flow Fields to PEM Fuel Cells and Cell Stack Performance". In: *Frontiers in Energy Research* 2 (Jan. 2014), pp. 1–8. ISSN: 2296-598X. DOI: 10.3389/fenrg.2014.00002.

[28] Kui Jiao, Jaewan Park, and Xianguo Li. "Experimental investigations on liquid water removal from the gas diffusion layer by reactant flow in a PEM fuel cell". In: *Applied Energy* 87.9 (2010), pp. 2770–2777. ISSN: 03062619. DOI: 10.1016/j.apenergy.2009.04.041.

[29] Xianguo Li, Imran Sabir, and Jaewan Park. "A flow channel design procedure for PEM fuel cells with effective water removal". In: *Journal of Power Sources* 163.2 (2007), pp. 933–942. ISSN: 03787753. DOI: 10.1016/j.jpowsour.2006.10.015.

[30] Nathanial J. Cooper et al. "Experimental optimization of parallel and interdigitated PEMFC flow-field channel geometry". In: *International Journal of Hydrogen Energy* 41 (2016), pp. 1213–1223. ISSN: 03603199. DOI: 10.1016/j.ijhydene.2015.11.153.

[31] Yasuyuki Sando. "Research and Development of Fuel Cell Vehicles at Honda". In: 25.1 (2010), pp. 211–224. DOI: 10.1149/1.3210573.

[32] T.A. Trabold et al. "In situ investigation of water transport in an operating PEM fuel cell using neutron radiography". In: *International Journal of Heat and Mass Transfer* 49.25-26 (2006), pp. 4712–4720. ISSN: 00179310. DOI: 10.1016/j.ijheatmasstransfer.2006.07.003.

[33] N. Pekula et al. "Study of water distribution and transport in a polymer electrolyte fuel cell using neutron imaging". In: *Nuclear Instruments and Methods in Physics Research, Section A: Accelerators, Spectrometers, Detectors and Associated Equipment* 542.1-3 (Apr. 2005), pp. 134–141. ISSN: 01689002. DOI: 10.1016/j.nima.2005.01.090.

[34] Dusan Spernjak, Ajay K. Prasad, and Suresh G. Advani. "In situ comparison of water content and dynamics in parallel, single-serpentine, and interdigitated flow fields of polymer electrolyte membrane fuel cells". In: *Journal of Power Sources* 195.11 (2010), pp. 3553–3568. ISSN: 03787753. DOI: 10.1016/j.jpowsour.2009.12.031.

[35] Yuh Ming Ferng and Ay Su. "A three-dimensional full-cell CFD model used to investigate the effects of different flow channel designs on PEMFC performance". In: *International Journal of Hydrogen Energy* 32.17 (Dec. 2007), pp. 4466–4476. ISSN: 03603199. DOI: 10.1016/j.ijhydene.2007.05.012.

[36] Yuxiu Liu et al. "Proton Conduction in PEM Fuel Cell Cathodes: Effects of Electrode Thickness and Ionomer Equivalent Weight". In: *Journal of The Electrochemical Society* 157.8 (Aug. 2010), B1154. ISSN: 00134651. DOI: 10.1149/1.3435323.

[37] W. Q. Tao et al. "Parameter sensitivity examination and discussion of PEM fuel cell simulation model validation. Part I. Current status of modeling research and model development". In: *Journal of Power Sources* 160.1 (Sept. 2006), pp. 359–373. ISSN: 03787753. DOI: 10.1016/j.jpowsour.2006.01.078.

[38] C. Siegel. "Review of computational heat and mass transfer modeling in polymer-electrolyte-membrane (PEM) fuel cells". In: *Energy* 33.9 (2008), pp. 1331–1352. ISSN: 03605442. DOI: 10.1016/j.energy.2008.04.015.

[39] Chao-Yang Wang. "Fundamental Models for Fuel Cell Engineering". In: *Chemical Reviews* 104.10 (2004), pp. 4727–4766. ISSN: 0009-2665. DOI: 10.1021/cr020718s.

[40] A. Ghanbarian and M. J. Kermani. "Enhancement of PEM fuel cell performance by flow channel indentation". In: *Energy Conversion and Management* 110 (2016), pp. 356–366. ISSN: 01968904. DOI: 10.1016/j.enconman.2015.12.036.

[41] E.H. Majlan et al. "Numerical analysis of modified parallel flow field designs for fuel cells". In: *International Journal of Hydrogen Energy* 42.14 (2016), pp. 9210–9218. ISSN: 03603199. DOI: 10.1016/j.ijhydene.2016.03.189.

[42] Chun H. Min. "Performance of a proton exchange membrane fuel cell with a stepped flow field design". In: *Journal of Power Sources* 186.2 (2009), pp. 370–376. ISSN: 03787753. DOI: 10.1016/j.jpowsour.2008.10.048.

[43] W. M. Yan et al. "Effects of flow distributor geometry and diffusion layer porosity on reactant gas transport and performance of proton exchange membrane fuel cells". In: *Journal of Power Sources* 125.1 (2004), pp. 27–39. ISSN: 03787753. DOI: 10.1016/j.jpowsour.2003.07.017.

[44] Y. Sui et al. "Fluid flow and heat transfer in wavy microchannels". In: *International Journal of Heat and Mass Transfer* 53.13-14 (2010), pp. 2760–2772. ISSN: 00179310. DOI: 10.1016/j.ijheatmasstransfer.2010.02.022.

[45] Tadashi Nishiyama. *Patent Application Publication Pub. No.: US 2014/0270163 A1*. 2011. DOI: 10.1016/j.(73). arXiv: arXiv:1208.5721.

[46] Minoru Matsunaga, Tatsuya Fukushima, and Kuniaki Ojima. "Powertrain system of Honda FCX clarity fuel cell vehicle". In: *World Electric Vehicle Journal* 3.4 (2009), pp. 820–829. ISSN: 20326653. DOI: May13–16.

[47] C Johnson. *(12) United States Patent*. 2003. DOI: 10.1145/634067.634234..

[48] Jenn Kun Kuo, Tzu Hsiang Yen, and Cha'o Kuang Chen. "Three-dimensional numerical analysis of PEM fuel cells with straight and wave-like gas flow fields channels". In: *Journal of Power Sources* 177.1 (2007), pp. 96–103. ISSN: 03787753. DOI: 10.1016/j.jpowsour.2007.11.065.

[49] Yue-Tzu Tzu Yang, Kuo-Teng Teng Tsai, and Cha'o-Kuang Cha'O Kuang Cha'o-Kuang Chen. "The Effects of the PEM Fuel Cell Performance with the Waved Flow Channels". In: *Journal of Applied Mathematics* 2013 (2013), pp. 1–14. ISSN: 1110-757X. DOI: 10.1155/2013/862645.

[50] Seong Ho Han, Nam Hyeon Choi, and Young Don Choi. "Simulation and experimental analysis on the performance of PEM fuel cell by the wave-like surface design at the cathode channel". In: *International Journal of Hydrogen Energy* 39.6 (2014), pp. 2628–2638. ISSN: 03603199. DOI: 10.1016/j.ijhydene.2013.08.063.

[51] Minkmas V. Williams et al. "Characterization of Gas Diffusion Layers for PEMFC". In: *Journal of The Electrochemical Society* 151.8 (2004), A1173–A1180. DOI: 10.1149/1.1764779. eprint: http://jes.ecsdl.org/content/151/8/A1173.full.pdf+html.

[52] M. Prasanna et al. "Influence of cathode gas diffusion media on the performance of the PEMFCs". In: *Journal of Power Sources* 131.1 (2004). Selected papers presented at the Eighth Grove Fuel Cell Symposium, pp. 147–154. ISSN: 0378-7753. DOI: https://doi.org/10.1016/j.jpowsour.2004.01.030.

[53] M F Mathias et al. "Diffusion media materials and characterisation". In: *Handbook of Fuel Cells* 3 (2010), pp. 517–537. DOI: 10.1002/9780470974001.f303046.

[54] Paolo Fracas et al. "Electrical Characterization of GDL Materials for Polymer Fuel Cells (PEMFC)". In: *ECS Transactions* 12.1 (2008), pp. 51–57. DOI: 10.1149/1.2921532. eprint: http://ecst.ecsdl.org/content/12/1/51.full.pdf+html.

[55] Kazuyoshi Fushinobu, Daishi Takahashi, and Ken Okazaki. "Micromachined metallic thin films for the gas diffusion layer of PEFCs". In: *Journal of Power Sources* 158 (2006). ISSN: 0378-7753.

[56] R Petričević, M Glora, and J Fricke. "Planar fibre reinforced carbon aerogels for application in PEM fuel cells". In: *Carbon* 39.6 (2001), pp. 857–867.

[57] M Glora et al. "Integration of carbon aerogels in PEM fuel cells". In: *Journal of non-crystalline solids* 285.1-3 (2001), pp. 283–287.

[58] A. Schmitz et al. "Planar self-breathing fuel cells". In: *Journal of Power Sources* 118.1-2 (2003), pp. 162–171. ISSN: 03787753. DOI: 10.1016/S0378-7753(03)00080-6.

[59] Woo-kum Lee et al. "The effects of compression and gas diffusion layers on the performance of a PEM fuel cell". In: *Journal of power sources* 84.1 (1999), pp. 45–51.

[60] David A. Caulk and Daniel R. Baker. "Modeling Two-Phase Water Transport in Hydrophobic Diffusion Media for PEM Fuel Cells". In: *Journal of The Electrochemical Society* 158.4 (2011), B384. ISSN: 00134651. DOI: 10.1149/1.3551504.

[61] D Bevers, R Rogers, and M Von Bradke. "Examination of the influence of PTFE coating on the properties of carbon paper in polymer electrolyte fuel cells". In: *Journal of power sources* 63.2 (1996), pp. 193–201.

[62] Christian Quick et al. "Characterization of water transport in gas diffusion media". In: *Journal of Power Sources* 190.1 (2009), pp. 110–120. ISSN: 03787753. DOI: 10.1016/j.jpowsour.2008.07.093.

[63] Toshikazu Kotaka et al. "The Analysis of Mass Transport Phenomena in Micro Porous Layer for High Current Density Operation in PEMFC for Automobile Application". In: *ASME 2013 11th Fuel Cell Science, Engineering and Technology Conference FuelCell2013*. 2013, pp. 1–9. DOI: 10.1115/FuelCell2013-18126.

[64] Ugur Pasaogullari and Chao-Yang Wang. "Two-phase transport and the role of micro-porous layer in polymer electrolyte fuel cells". In: *Electrochimica Acta* 49.25 (2004), pp. 4359–4369.

[65] Hironori Nakajima, Toshiaki Konomi, and Tatsumi Kitahara. "Direct water balance analysis on a polymer electrolyte fuel cell (PEFC): Effects of hydrophobic treatment and micro-porous layer addition to the gas diffusion layer of a PEFC on its performance during a simulated start-up operation". In: *Journal of Power Sources* 171.2 (2007), pp. 457–463.

[66] Md Azimur Rahman et al. "Development of 1-D multiphysics PEMFC model with dry limiting current experimental validation". In: *Electrochimica Acta* (2019), p. 134601.

[67] Bryon R. Bird, Warren E. Stewart, and Edwin N. Lightfoot. *Transport Phenomena*. John Wiley & Sons, 2002. ISBN: 978-81-265-0808-2.

[68] Ryosuke Jinnouchi et al. "Molecular dynamics simulations on O2 permeation through Nafion ionomer on platinum surface". In: *Electrochimica Acta* 188 (2016), pp. 767–776.

[69] Anusorn Kongkanand and Mark F. Mathias. "The Priority and Challenge of High-Power Performance of Low-Platinum Proton-Exchange Membrane Fuel Cells". In: *Journal of Physical Chemistry Letters* 7.7 (2016), pp. 1127–1137. ISSN: 19487185. DOI: 10.1021/acs.jpclett.6b00216.

[70] Alessandro Zana et al. "Accessing the inaccessible: analyzing the oxygen reduction reaction in the diffusion limit". In: *ACS applied materials & interfaces* 9.44 (2017), pp. 38176–38180.

[71] Dusan Spernjak et al. “Enhanced Water Management of Polymer Electrolyte Fuel Cells with Additive-Containing Microporous Layers”. In: *ACS Applied Energy Materials* 1.11 (2018), pp. 6006–6017.

[72] Nideld, Donald A. and Bejan, Adrian. *Convection in Porous Media*. Springer International Publishing, 2017. ISBN: 978-3-319-49561-3. DOI: 10.1007/978-3-49562-0.

[73] Sunden, B. and Faghri, M. *Transport phenomena in fuel cells*. WIT Press, 2005. ISBN: 978-1-85312-840-0.

[74] R Lenormand. “Liquids in porous media”. In: *Journal of Physics: Condensed Matter* 2.S (Dec. 1990), SA79–SA88. DOI: 10.1088/0953-8984/2/s/008.

[75] FY Zhang, XG Yang, and CY Wang. “Liquid water removal from a polymer electrolyte fuel cell”. In: *Journal of the Electrochemical Society* 153.2 (2006), A225–A232.

[76] EC Kumbur, KV Sharp, and MM Mench. “Liquid droplet behavior and instability in a polymer electrolyte fuel cell flow channel”. In: *Journal of Power Sources* 161.1 (2006), pp. 333–345.

[77] Ken S. Chen, Michael A. Hickner, and David R. Noble. “Simplified models for predicting the onset of liquid water droplet instability at the gas diffusion layer/gas flow channel interface”. In: *International Journal of Energy Research* 29.12 (2005), pp. 1113–1132. ISSN: 0363907X. DOI: 10.1002/er.1143.

[78] Christoph Simon, Frederic Hasch, and Hubert A Gasteiger. “Influence of the Gas Diffusion Layer Compression on the Oxygen Transport in PEM Fuel Cells at High Water Saturation Levels”. In: *Journal of The Electrochemical Society* 164.6 (2017), F591–F599. ISSN: 0013-4651. DOI: 10.1149/2.0691706jes.

[79] Dietmar Gerteisen et al. “Effect of operating conditions on current density distribution and high frequency resistance in a segmented PEM fuel cell”. In: *International Journal of Hydrogen Energy* 37.9 (2012), pp. 7736–7744. ISSN: 03603199. DOI: 10.1016/j.ijhydene.2012.02.024.

[80] Tae Hyun Kim et al. “Solvent effect on the Nafion agglomerate morphology in the catalyst layer of the proton exchange membrane fuel cells”. In: *International Journal of Hydrogen Energy* 42.1 (2017), pp. 478–485. ISSN: 03603199. DOI: 10.1016/j.ijhydene.2016.12.015.

[81] E. Birgersson, M. Noponen, and M. Vynnycky. “Analysis of a Two-Phase Non-Isothermal Model for a PEFC”. In: *Journal of The Electrochemical Society* 152.5 (2005), A1021. ISSN: 00134651. DOI: 10.1149/1.1877992.

[82] M. Grujicic and K. M. Chittajallu. "Design and optimization of polymer electrolyte membrane (PEM) fuel cells". In: *Applied Surface Science* 227.1-4 (2004), pp. 56–72. ISSN: 01694332. DOI: 10.1016/j.apsusc.2003.10.035.

[83] Galip H. Guvelioglu and Harvey G. Stenger. "Computational fluid dynamics modeling of polymer electrolyte membrane fuel cells". In: *Journal of Power Sources* 147.1-2 (2005), pp. 95–106. ISSN: 03787753. DOI: 10.1016/j.jpowsour.2005.01.011.

[84] Wei Sun, Brant A. Peppley, and Kunal Karan. "An improved two-dimensional agglomerate cathode model to study the influence of catalyst layer structural parameters". In: *Electrochimica Acta* 50.16-17 (2005), pp. 3359–3374. ISSN: 00134686. DOI: 10.1016/j.electacta.2004.12.009.

[85] Hanxia Ruan et al. "Design and simulation of novel flow field plate geometry for proton exchange membrane fuel cells". In: *Heat and Mass Transfer* 52.10 (2016), pp. 2167–2176. ISSN: 1432-1181. DOI: 10.1007/s00231-015-1737-6.

[86] Rohit Makharia, Mark F. Mathias, and Daniel R. Baker. "Measurement of Catalyst Layer Electrolyte Resistance in PEFCs Using Electrochemical Impedance Spectroscopy". In: *Journal of The Electrochemical Society* 152.5 (2005), A970. ISSN: 00134651. DOI: 10.1149/1.1888367.

[87] Yuhao Lu and Ramana G. Reddy. "Performance of micro-PEM fuel cells with different flow fields". In: *Journal of Power Sources* 195.2 (2010), pp. 503–508. ISSN: 03787753. DOI: 10.1016/j.jpowsour.2009.07.003.

[88] N Pekula et al. "Study of water distribution and transport in a polymer electrolyte fuel cell using neutron imaging". In: *Nuclear Instruments and Methods in Physics Research, Section A: Accelerators, Spectrometers, Detectors and Associated Equipment*. Vol. 542. 1-3. 2005, pp. 134–141. DOI: 10.1016/j.nima.2005.01.090.

[89] Irfan S. Hussaini and Chao Yang Wang. "Visualization and quantification of cathode channel flooding in PEM fuel cells". In: *Journal of Power Sources* 187.2 (2009), pp. 444–451. ISSN: 03787753. DOI: 10.1016/j.jpowsour.2008.11.030.

[90] Jennifer Peron et al. "Properties of Nafion® NR-211 membranes for PEMFCs". In: *Journal of Membrane Science* 356.1-2 (2010), pp. 44–51.

[91] Wei Mon Yan et al. "Effects of operating temperatures on performance and pressure drops for a 256 cm2 proton exchange membrane fuel cell: An experimental study". In: *Journal of Power Sources* 185.2 (2008), pp. 1040–1048. ISSN: 03787753. DOI: 10.1016/j.jpowsour.2008.08.053.

[92] Elisabetta Arato et al. “Gas-phase mass-transfer resistances at polymeric electrolyte membrane fuel cells electrodes: Theoretical analysis on the effectiveness of interdigitated and serpentine flow arrangements”. In: *Energies* 9.4 (2016). ISSN: 19961073. DOI: 10.3390/en9040229.

[93] Shou Shing Hsieh, Yi Ji Huang, and Bing Shyan Her. “Pressure drop on water accumulation distribution for a micro PEM fuel cell with different flow field plates”. In: *International Journal of Heat and Mass Transfer* 52.23-24 (2009), pp. 5657–5659. ISSN: 00179310. DOI: 10.1016/j.ijheatmasstransfer.2009.07.010.

[94] D. Tehlar et al. “Investigation of channel-to-channel cross convection in serpentine flow fields”. In: *Fuel Cells* 10.6 (2010), pp. 1040–1049. ISSN: 16156846. DOI: 10.1002/fuce.201000034.

[95] Xianguo Li and Imran Sabir. “Review of bipolar plates in PEM fuel cells: Flow-field designs”. In: *International Journal of Hydrogen Energy* 30.4 (2005), pp. 359–371. ISSN: 03603199. DOI: 10.1016/j.ijhydene.2004.09.019.

[96] Daniel R Baker et al. “The Use of Limiting Current to Determine Transport Resistance in PEM Fuel Cells”. In: *ECS Transactions* 3.1 (2006), pp. 989–999. ISSN: 19385862. DOI: 10.1149/1.2356218.

[97] T. A. Greszler, D. Caulk, and P. Sinha. “The Impact of Platinum Loading on Oxygen Transport Resistance”. In: *Journal of the Electrochemical Society* 159.12 (2012), F831–F840. ISSN: 0013-4651. DOI: 10.1149/2.061212jes.

[98] Hwanyeong Oh et al. “Experimental dissection of oxygen transport resistance in the components of a polymer electrolyte membrane fuel cell”. In: *Journal of Power Sources* 345 (2017), pp. 67–77. ISSN: 03787753. DOI: 10.1016/j.jpowsour.2017.01.087.

[99] Daniel R. Baker et al. “Measurement of Oxygen Transport Resistance in PEM Fuel Cells by Limiting Current Methods”. In: *Journal of The Electrochemical Society* 156.9 (2009), B991. ISSN: 00134651. DOI: 10.1149/1.3152226.

[100] Hui Li et al. “A review of water flooding issues in the proton exchange membrane fuel cell”. In: *Journal of Power Sources* 178.1 (2008), pp. 103–117. ISSN: 03787753. DOI: 10.1016/j.jpowsour.2007.12.068.

[101] A Forner-Cuenca et al. “Advanced water management in PEFCs: diffusion layers with patterned wettability II. Measurement of capillary pressure characteristic with neutron and synchrotron imaging”. In: *Journal of The Electrochemical Society* 163.9 (2016), F1038–F1048.

[102] Jon P. Owejan, Thomas A. Trabold, and Matthew M. Mench. "Oxygen transport resistance correlated to liquid water saturation in the gas diffusion layer of PEM fuel cells". In: *International Journal of Heat and Mass Transfer* 71 (2014), pp. 585–592. ISSN: 00179310. DOI: 10.1016/j.ijheatmasstransfer.2013.12.059.

[103] Zuoxiang Zhang et al. "Gas convection in fuel cells: An overlooked factor". In: *Electrochimica Acta* 176 (2015), pp. 1476–1483. ISSN: 00134686. DOI: 10.1016/j.electacta.2015.07.087.

[104] Charles H Schillberg. "A Review of Models for Water Droplet Detachment From the Gas Diffusion Layer-Gas Flow Channel Interface in PEMFCs". In: *ASME 5th International Conference on Nanochannels, Microchannels, and Minichannels*. 2007, pp. 1–12. DOI: 10.1115/ICNMM2007-30029.

[105] Xiaozi Yuan et al. "AC impedance technique in PEM fuel cell diagnosis-A review". In: *International Journal of Hydrogen Energy* 32.17 (2007), pp. 4365–4380. ISSN: 03603199. DOI: 10.1016/j.ijhydene.2007.05.036.

[106] Xiaozi Yuan et al. "AC impedance diagnosis of a 500 W PEM fuel cell stack. Part I: Stack impedance". In: *Journal of Power Sources* 161.2 (2006), pp. 920–928. ISSN: 03787753. DOI: 10.1016/j.jpowsour.2006.05.003.

[107] Xiao-Zi Yuan. *Electrochemical Impedance Spectroscopy in PEM Fuel Cells: Fundamentals and Applications*. Springer, 2009.

[108] Mariana Ciureanu and Raymond Roberge. "Electrochemical impedance study of PEM fuel cells. Experimental diagnostics and modeling of air cathodes". In: *The Journal of Physical Chemistry B* 105.17 (2001), pp. 3531–3539.

[109] Robert N Carter et al. "Artifacts in measuring electrode catalyst area of fuel cells through cyclic voltammetry". In: *Ecs Transactions* 11.1 (2007), pp. 403–410.

[110] *FREUDENBERG GAS DIFFUSION LAYERS TECHNICAL DATA*. 2017.

[111] *Toray Carbon Fiber Paper "THP-H"*. Fuel Cell Store.

[112] Rudiger Schweiss et al. *Sigracet gas Diffusion Layers for PEM Fuel Cells, Electrolyzers and Batteries*. SGL Carbon GmbH, 2016.